Master's Thesis

Improved structural stability of Ni-rich cathode materials via simple dry process for Li-ion Batteries

Jieun Lee

Department of Energy Engineering

(Battery Science and Technology)

Graduate School of UNIST

2017

Improved structural stability of Ni-rich cathode materials via simple dry process for Li-ion Batteries

Jieun Lee

Department of Energy Engineering

(Battery Science and Technology)

Graduate School of UNIST

Improved structural stability of Ni-rich cathode materials via simple dry process for Li-ion Batteries

A thesis/dissertation

submitted to the Graduate School of UNIST

in partial fulfillment of the

requirements for the degree of

Master of Science

Jieun Lee

7. 1. 2017 of submission

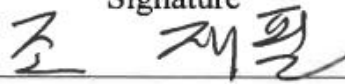Approved by
_____

Advisor

Jaephil Cho

Improved structural stability of Ni-rich cathode materials via simple dry process for Li-ion Batteries

Jieun Lee

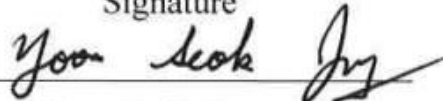This certifies that the thesis/dissertation of Jieun Lee is approved.
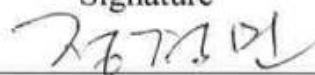
7. 1. 2017

Signature

Advisor: Jaephil Cho

Signature

Yoon Seok Jung

Signature

Kyeong-Min Jeon

Abstract

I reported that highly stable $LiNi_{0.8}Co_{0.1}Mn_{0.1}O_2$ (that is, NCM) via a simple and one-step dry surface treatment approach (that is, G-NCM). The cobalt precursor was coated on the surface of the bare NCM in purpose to improve the material integrity by protecting the cathode surface against the acidic species attack. Furthermore, the transition metal (TM) concentration gradient in the primary particles ensured the structural stability by suppressing the evolution of micro-crack in the cathode particles and reducing transition metal dissolution. The more important thing was the enhanced material integrity allowed stable and uniform solid electrolyte interphase (SEI) layer on the graphite anode, leading to unprecedented full-cell performance.

After the surface treatment, the high temperature (45 °C) cycle performance was improved from 20 % for bare NCM to 50 % for G-NCM. During the cycle, the G-NCM retained higher average coulombic efficiency of ~99.8 % than that of the bare NCM (~98.5 %). The electrochemical performance was prepared by full-cell. This finding could be a breakthrough for the LIB technology, providing a rational approach for the development of advanced cathode materials.

Contents

List of figures

Nomenclature

LIB	Lithium-ion Battery
CV	Cyclic Voltammetry.
FCC	Face-Centered Cubic
XRD	X-ray Diffraction Analysis
TGA	Thermogravimetric Analysis
DSC	Differential Scanning Calorimetry
CSTR	Continuous Stirred Tank Reactor
SEM	Scanning Electron Microscope
TEM	Transmission Electron Microscopy
HR-TEM	High-resolution Transmission Electron Microscopy
STEM	Scanning Transmission Electron Microscopy
FIB	Focused Ion Beam
TOF-SIMS	Time of Flight Secondary Ion Mass Spectrometry
EDS	Energy Dispersive Spectrometer
DC-IR	Direct Current Internal Resistance

I. Introduction

1.1 Lithium-ion battery

Lithium-ion battery was firstly commercialized in 1991 by SONY. The cathode material is $LiCoO_2$ and the anode material is carbonaceous material, for example, graphite.[1] Lithium-ion battery can convert chemical energy to electric energy. In other words, it can store electric energy as chemical energy. It is not a single-use battery (= primary battery) but rechargeable battery (= secondary battery) which lithium ions move from the anode to the cathode during discharge and back when charge.[2] Lithium-ion battery is consist of 4 main components, the cathode, anode, separator and the electrolyte. A separator is a physical barrier between two electrodes. It must be permeable to the ions and inert in the battery system. An electrolyte provides pure ionic conductivity between two electrodes of a cell. Main electrochemical reactions are occurred at the cathode and anode. Oxidation-reduction reaction during charging and discharging at both electrodes are followed.[3]

$$\text{Cathode electrode: } LiCoO_2 \leftrightarrow Li_{1-x}CoO_2 + xLi^+ + xe^-$$

$$\text{Anode electrode: } C_6 + xLi^+ + xe^- \leftrightarrow Li_xC_6$$

$$\text{Overall reaction: } LiCoO_2 + C_6 \leftrightarrow Li_{1-x}CoO_2 + Li_xC_6$$
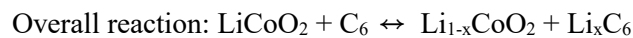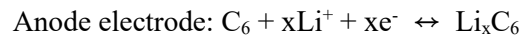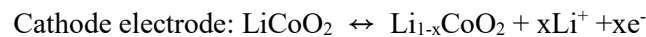
$$\rightarrow \text{ : charge process}$$

$$\leftarrow \text{ : discharge process}$$

In charge process, $LiCoO_2$ which is the cathode material is oxidized to $Li_{1-x}CoO_2$ by losing both Li^+ ion and electron. At the same time C_6 (graphite) which is the anode material is reduced to Li_xC_6 by gaining both Li^+ ion and electron. In discharge process, all reactions are reversed.
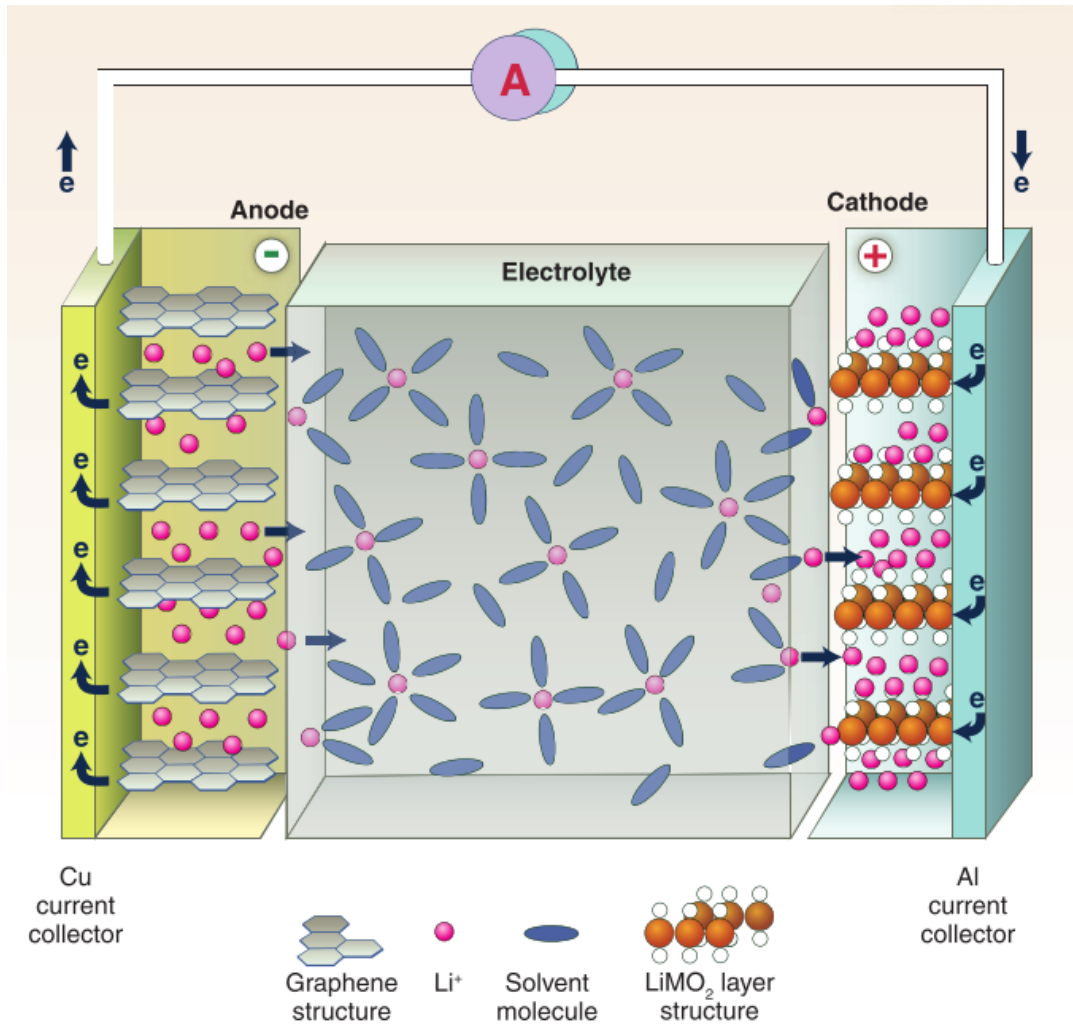
Figure 1. Schematic illustration of a $Li_{1-x}MO_2/Li_xC_6$ Lithium-ion Battery.[3]

1.2 Ni-rich cathode materials for lithium-ion battery

1.2.1 LiNiO$_2$

Cathode is one of the most important parts of the lithium-ion battery and commonly it has a metal oxide framework. Lithium ion is contained in a metal oxide framework and it can move into anode and back to original site. Cathode can be divided into three types by their structure. Layered, spinel and olivine structure. The crystal structures of the cathode materials are shown in Figure 2. Commercially used LiCoO$_2$ and LiNiO$_2$ are layered structure, LiMn$_2$O$_4$ is spinel structure and LiFePO$_4$ is known for Olivine structure.[4]

The layered cathode materials such as LiMO$_2$ is consisted of lithium ions, transition metal ions (M = Co, Ni, Mn, etc.) and oxygen ions.[5] It has α-NaFeO$_2$ crystal structure and belongs to the R$\bar{3}$m space group with FCC structure (ABC type stacking) of the oxygen ion. The transition metal, M^{3+} ion is coordinated by six O^{2-} ions and the MO$_6$ form a layer along x and y directions. The lithium ions and transition metal ions are located at octahedral sites and makes alternate planes, where transition metal layers are called TM slab (transition metal slab) and lithium ions can be inserted and extracted between TM slabs thus also forms lithium ion slab which is called Li slab. In other words, R$\bar{3}$m space group which stacking like O-Li-O-TM–O–Li-TM-O along the [111] face and lithium ions show 2-dimensional diffusion along the Li slab.[6]

a) Layered LiCoO$_2$ & LiNiO$_2$ b) Spinel LiMn$_2$O$_4$ c) Olivine LiFePO4
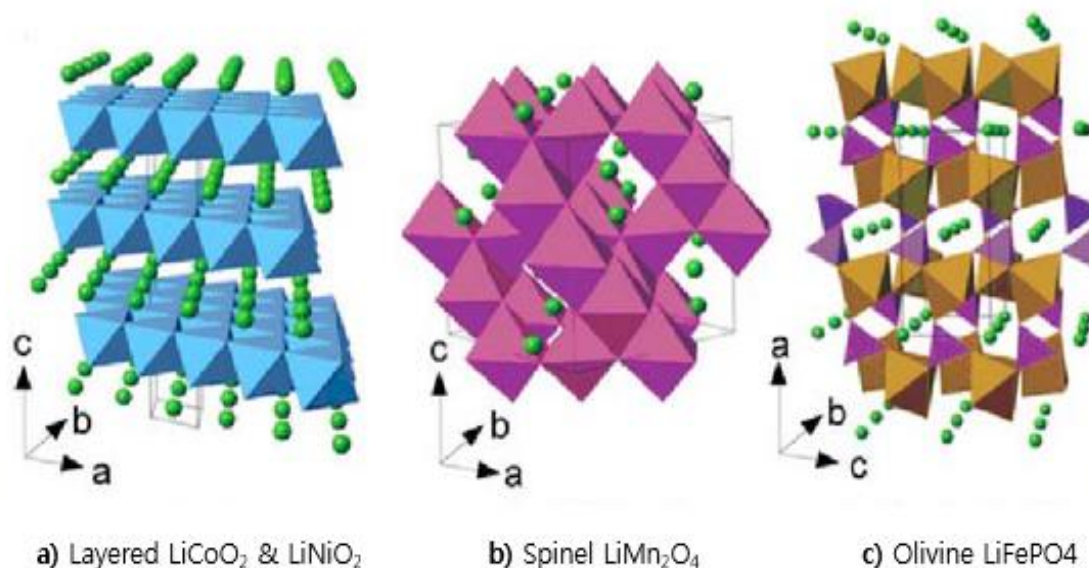
Figure 2. The crystal structures of **a)** layered structure, **b)** spinel structure and **c)** olivine structure.[7]

3

The LiNiO$_2$ material is attractive as a cathode material with higher theoretical capacity and lower cost than LiCoO$_2$.[8] The first report on the electrochemical properties of LiNiO$_2$ was published in 1985 by M. G. S. R. It is classed as layered sturcture cathode material. The main problem of LiNiO$_2$ is nonstoichiometry. Nonstoichiometry is natural phenomenon of LiNiO$_2$ which causes other severe problems.

The electronic structure of LiNiO$_2$ in Figure 3 is an evidence that LiNiO$_2$ has higher capacity than LiCoO$_2$.[9] Theoritically, only 50% of the theoretical capacity of LiCoO$_2$ could be utilized in lithium ion cells. This corresponds to a reversible insertion and extraction of 0.5 lithium in Li$_x$CoO$_2$ a significant overlap of the redox active Co$^{3+/4+}$ O2 :2p band. On the other hand, the redox active Ni$^{3+/4+}$: e$_g$ band only hardly touches the top of the O^{2-} :2p band in Li$_x$NiO$_2$. The Ni^{4+} state can be achieved in a layered material with much higher utilization of lithium in the host structure.

Figure 4 and Figure 5 shows various structural transformation of LiNiO$_2$ during electrochemical process.[10] The Li$_x$NiO$_2$ ($0 \leq x \leq 1$) exhibits phase transition on charge process. The structure of LiNiO$_2$ is changed from O3 to M, M to H1-3 and H1-3 to O1 (O3, M1, H2, H3 are characterized by AB-CA-BC oxygen packing, while O1 is characterized by AB oxygen packing.). The phase transition into H3 is irreversible reaction and interrupts insertion and extraction of Li ions. Therefore, utilization of lithium in Li$_x$NiO$_2$ is the range of $0.3 < x < 1$ and the capacity is about 210mAh g^{-1}.
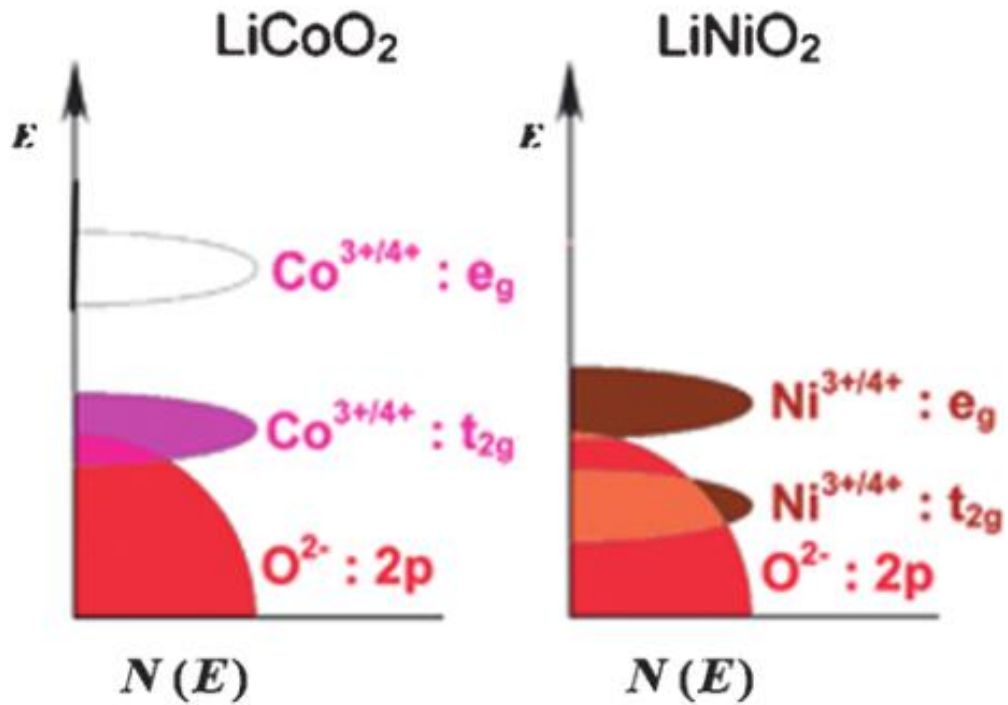
Figure 3. The electronic structure of $LiCoO_2$ and $LiNiO_2$.[9]
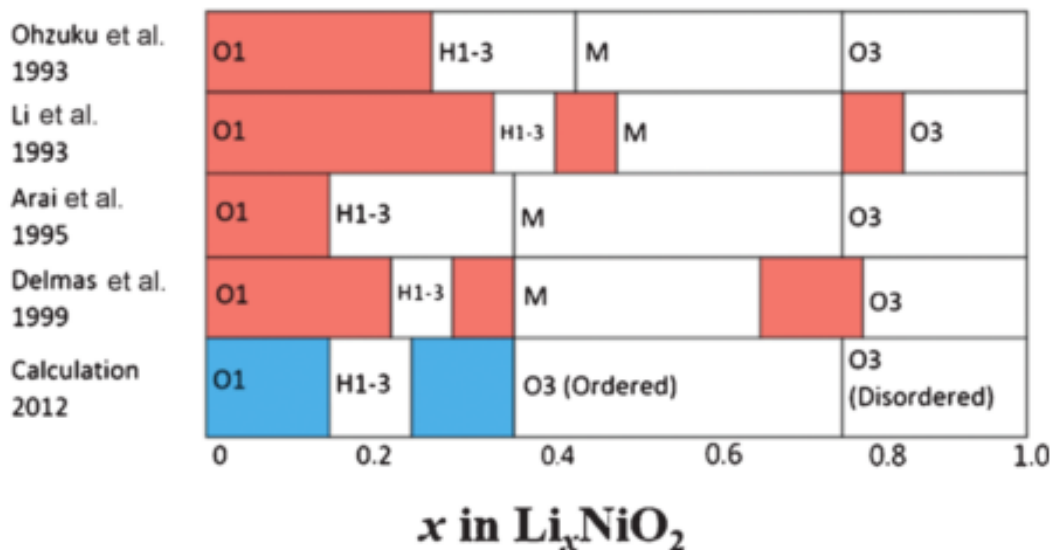
Figure 4. Phase diagram of the $LiNiO_2 \cdot NiO_2$ pseudo·binary system from experimental data (XRD) and calculation (ab initio).[10c, 11]
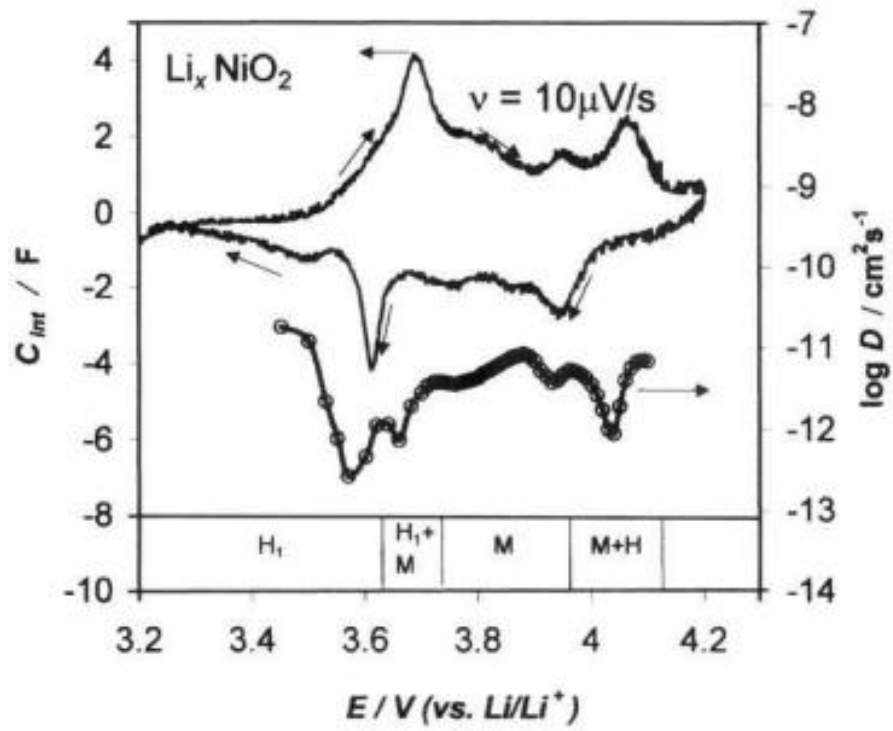
Figure 5. The general CV response of the LiNiO$_2$[12].

1.2.2 Nonstoichiometry

The LiNiO$_2$ is promising cathode material followed commercially used LiCoO$_2$ cathode material. To apply LiNiO$_2$ to cathode material, it needs to overcome some drawbacks. The main drawback of LiNiO$_2$ is non-stoichiometric structure which leads to several problems.[13] LiNiO$_2$ have solid solution between the layered structure and a disordered rock salt structure with the formula Li$_z$Ni$_{2-x}$O$_2$. J. R. Dahn and J. N. Reimers reported the Li$_x$Ni$_{x2-x}$O$_2$ structure for $0 \leq x \leq 1$. Li$_x$Ni$_{x2-x}$O$_2$ has a disordered rock salt structure for x<0.62 and Li and Ni atoms segregate into each layers for $0.62 \leq x \leq 1.0$.

Original layered materials have R$\overline{3}$m structure, which is repeating O-Li-O-TM-O along the rhombohedral [001] direction. Transition metal slab and lithium slab are clearly separated in perfect LiNiO$_2$ structure. According to crystal-filed theory, Ni^{3+} is unstable due to the unpaired electron spin of the e orbitals. Therefore Ni^{3+} has tendency to be oxidized to Ni^{2+} in transition metal site. The non-stoichiometric structure leads to partial reduction of nickel ion and the partial reduction causes structure collapse of the interlayer space, and transition metal ions migrate from the transition metal slab to the lithium slab. The ionic radius of Ni^{2+} (0.69Å) is similar to the ionic radius of Li$^+$ (0.76Å). It means Ni^{2+} ions easily move into Li$^+$ site in the Li slab. Migration of transition metal from TM site to Li site is called "cation mixing".[14] LiNiO$_2$ involves several phase transitions which is closely related to cation mixing.

Because of the smaller distance between the Li slab and TM slab in the disordered phase, it has a higher activation energy barrier than the ordered phase for diffusion of Li ion. Also, the disordered phase has a lower Li ion diffusivity due to hindrance which caused by the TM in the Li slab.[15] Therefore, increase of the cation mixing causes decrease of the rate capability of the cathode material. So, the degree of cation mixing is important role to predict a cell performance. To measure the degree of cation mixing, X-ray diffraction (XRD) analysis is commonly used.[12] Cation mixing is defined as the migration of transition metal ions from TM site to Li site (in Figure 6 c)). Cation mixing leads to a partial destructive interference of constructive interference of the (003) plane at a Bragg angle of $\theta_{d(003)}$. So intensity of the (003) peak decreases by cation mixing. Contrariwise, intensity of the (104) peak increases. On the (104) plane, transition metal ions in Li slab lead to increase of constructive interference of (104) plane. As a result, the ratio of the intensity of (003)/(104) peak decreases by increasing the degree of cation mixing.[16]
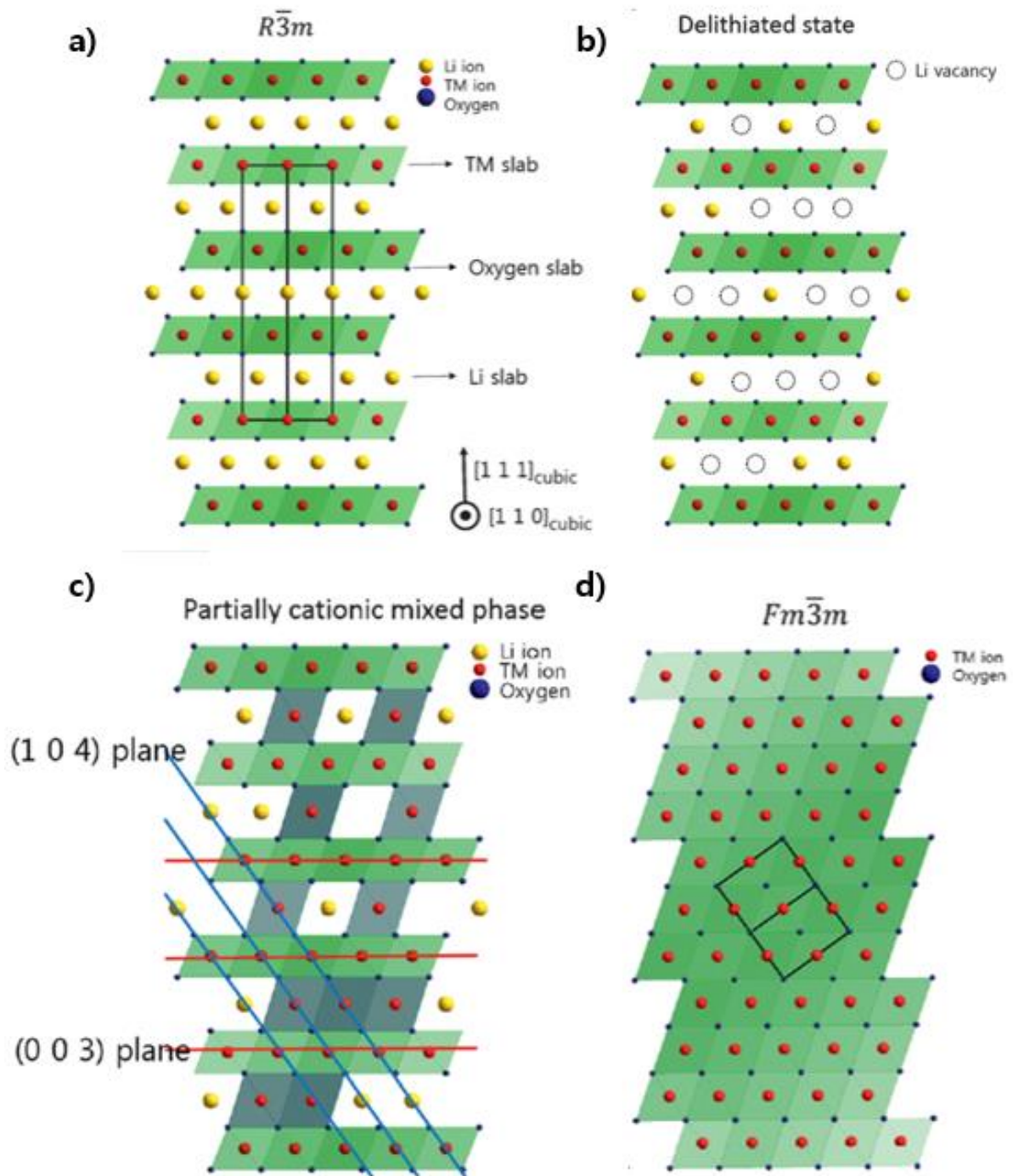
Figure 6. Structure of layered lithium metal oxide **a)** well ordered R$\bar{3}$m structure **b)** R$\bar{3}$m structure with Li vacancies at charged state **c)** Partially cation mixed phase with TM ions in Li slab. **d)** The cation mixing phase with Fm$\bar{3}$m structure. Li atoms are yellow, transition metals are red and oxygen atoms are dark[16a].

Phase transitions become more severe as the electrochemical cycling process proceeds.[15, 17] During the lithiation and delithiation process, $LiNiO_2$ undergoes degradation reactions such as structural change, side reaction with electrolyte. The layered structure changes into cation mixed structure or uncertain spinel phases because of oxygen release. The structure of $LiNiO_2$ is changed from a layered structure ($R\bar{3}m$) to a disordered spinel structure ($Fd\bar{3}m$) and finally changed into a rock-salt structure ($Fm\bar{3}m$). Process of phase transition is followed:

Charging (delithiation) → Extraction of Li^+ → Instable delithiated state → Reduction of transition metal → Oxygen evolution to maintain charge neutrality → Phase transition

Thermal stability is one of the most important consideration for choosing cathode material.[18] The thermal stability of the cathode material is closely related to oxygen evolution. J.R Dahn group reported charged Li_xNiO_2 (x <1) is unstable at high temperatures.[19] Oxygen can escape FCC structure and move into a heated electrolyte. Finally heated electrolyte over its flash point, leading to a violent reaction. The amount of escaped oxygen increases as x decreased in Li_xNiO_2.

Thermogravimetric analysis (TGA) result of a series of Li_xNiO_2 samples shows structure change of $LiNiO_2$ depending on the degree of charge (Figure 7). The large peak near 230°C decreases as x increases and is missing for x=0.5. The structure of Li_xNiO_2(x<0.5) convert to spinel structure ($LiNi_2O_4$) at 200℃ because of more than 4 oxygen atoms for 3 cations in x<0.5 samples. Differential Scanning Calorimetry (DSC) results of $LiNiO_2$ and $LiCoO_2$ which charged to various voltages are shown in Figure 8.[20] DSC profiles of $LiCoO_2$ is indicated as dashed lines at indicated voltages for comparison and the capacity of $LiCoO_2$ is shown near its respective graph. $LiNiO_2$ shows still more thermal instability the $LiCoO_2$. Because the Li_xNiO_2 samples show lower onset temperature and release more heat than Li_xCoO_2. At high voltage above 4.4 V, large exothermic peak is shown at $LiNiO_2$ which is much larger than the peak of $LiCoO_2$. Although, $LiNiO_2$ has higher capacity than $LiCoO_2$ at same voltage, the improvement of thermal stability is needed to use $LiNiO_2$.
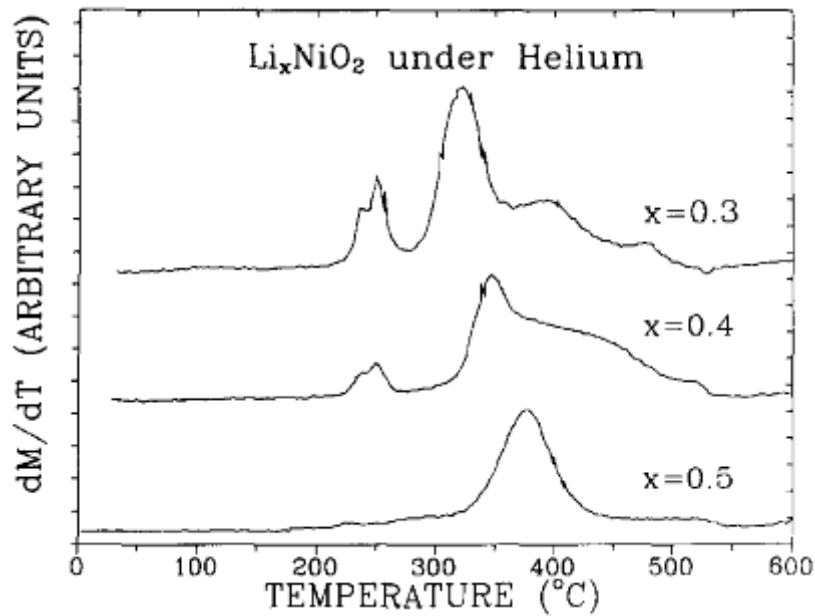
Figure 7. The derivatiive, dM/dT, versus temperature calculated from Thermogravimetric analysis (TGA) measurements on samples of Li_xNiO_2 with x=0.3, 0.4, and 0.5, as indicated[19].
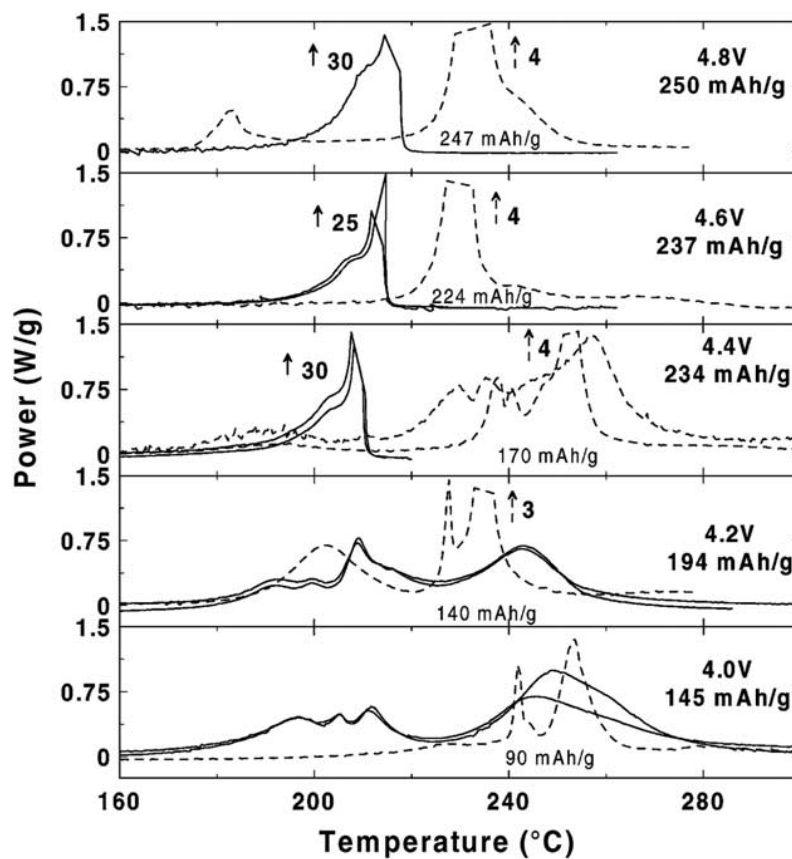
Figure 8. Differential Scanning Calorimetry (DSC) results of $LiNiO_2$ charged to indicated voltages. The results of $LiCoO_2$ are shown as dashed lines at the indicated voltage[20].

The other problem of $LiNiO_2$ is residual lithium.[21] During synthesis of Ni-rich cathode, lithium deficient nonstoichiometic lithium nickel oxide induces residual lithium (=free lithium).[10b, 17a] Residual lithium makes a PH of slurry higher and causes side reaction with electrolyte and gas evolution. As a result, capacity fading occurs.[22] Also exposure of air and moisture induces residual lithium compound (Li_2CO_3, LiOH). Those reactions are followed[23] :

$$LiNiO_2 + 1/2xCO_2 + 1/4xO_2 \rightarrow Li_{1-x}NiO_2 + 1/2Li_2CO_3$$
$$LiNiO_2 + yH_2O \rightarrow Li_{1-y}NiO_2 + yLiOH$$
$$2LiOH + CO_2 \rightarrow Li_2CO_3 + H_2O$$
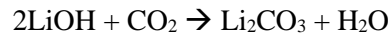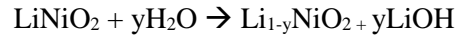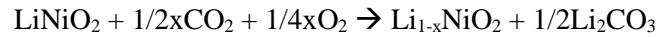
The cut-off voltage is generally above 4.3V in Lithium-ion battery. At the voltage range of 4.1 V~4.2 V, residual lithium compound lead to severe cell swelling.

$$2Li_2CO_3 + 4e^- \rightarrow 2CO_2 + O_2 + 4Li^+,$$
$$Li_2CO_3 + 2H^+ \rightarrow CO_2 + H_2O + 2Li^+$$
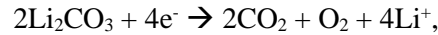
The $LiPF_6$ which is commonly used for electrolyte salt is unstable in H_2O and specially more unstable at high voltage and high temperature. Followed equations are the decomposition process of $LiPF_6$. Insulating LiF which is formed by decomposition of $LiPF_6$ is accumulated on the surface of active material. Residual lithium generates more amount of H_2O in electrolyte, and this accelarates the decomposition of the salt. Also the presence of residual lithium tends to bond with hydrocarbons induced from decomposition of electrolytic salt during electrochemical reactions. As a result, side reactions are more accelarated[24].

$$LiPF_6 \rightarrow LiF \downarrow + PF_5$$
$$PF_5 + H_2O \rightarrow POF_3 + _2 HF$$
$$POF_3 + 3 Li2O- \rightarrow 6 LiF \downarrow + P_2O_5 \downarrow (or Li_xPOF_y)$$

11
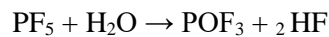
Figure 9. Schematic illustration of **a)** surface changes of $LiNiO_2$ after exposure in air and **b)** effect of the residual lithium on the surface of $LiNiO_2$[21b].

To obtain stable layered structure of $LiNiO_2$ without cation disorder, various elements are partially substituted to nickel sites such as $LiNiMnO_2$, $LiNiCoO_2$, $LiNiCoMnO_2$, and $LiNiCoAlO_2$[25,26]. These Ni based cathode materials called as Ni-rich cathode materials.[27] The synthesis method of Ni-rich cathode material, Co-precipitation method, is more complex than the synthesis method of $LiCoO_2$. $M(OH)_2$ precursor (M = Ni, Co, Mn, etc) is synthesized by co-precipitation and mixed with Li source such as Li carbonate or Li hydroxide and finally annealed at certain temperature. The three transitions metal layered for cathode materials to get each $LiMO_2$ led to the discovery of $LiNi_{1-x-y}Co_xMn_yO_2$ which were first published in 1999 by Liu. The electrochemical and physical properties of Ni-based cathode materials depend on the ratio of the elements in mixed compositions. If the increase of the ratio of cobalt causes decrease of capacity, increase of the nickel causes cation mixing and manganese causes phase transition from a layered phase to a spinel phase.

Nickel and cobalt based layered materials such as $LiNi_{1-x}Co_xO_2$ have been studied.[17a, 28] In $LiNi_{1-x}Co_xO_2$, the operating voltage increase as increases the x (the ratio of cobalt component). Because redox voltage of Co is higher than that of Ni for $MO_2/LiMO_2$ in $LiMO_2$. Cobalt substitution diminishes cation mixing. It provides the lithium pathway in a layered structure and improves the conductivity of the materials. Also nickel and manganese based layered-cathode materials such as $LiNi_{1-x}Mn_xO_2$ have been studied.[29] In $LiNi_{1-x}Mn_xO_2$, the the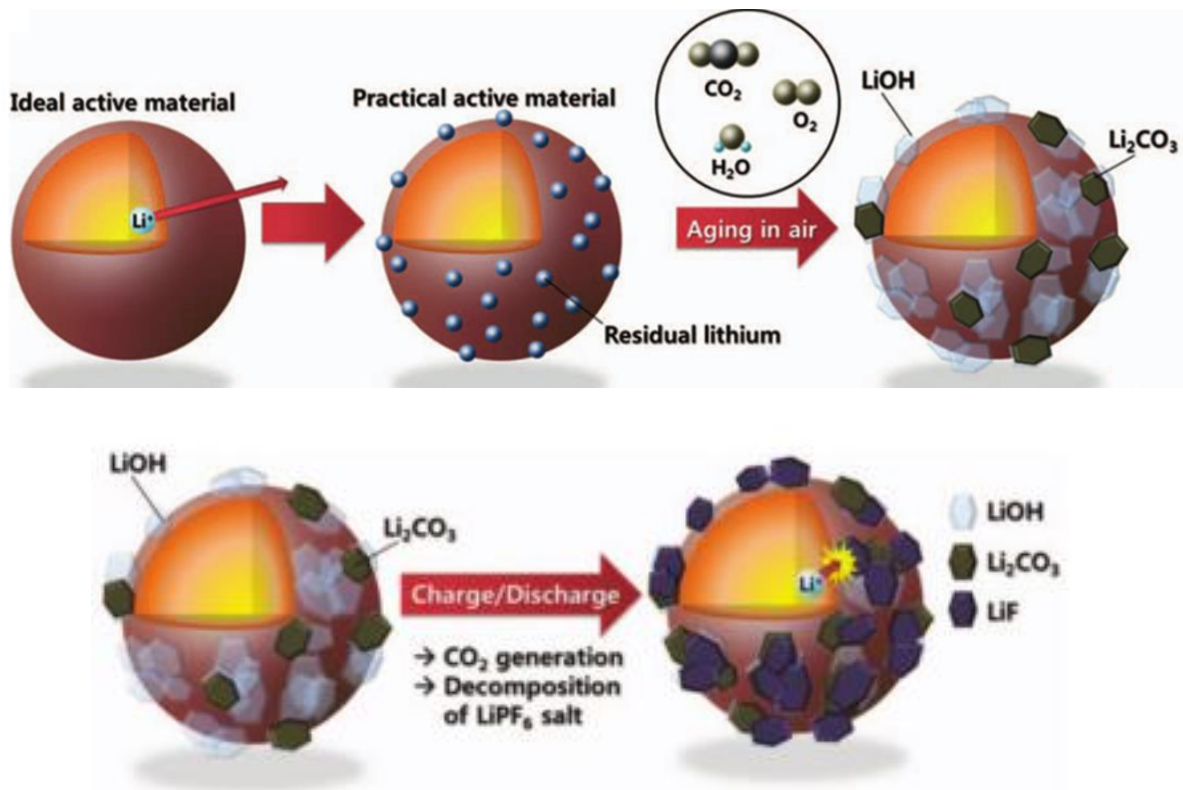rmal stability increase as increases the x (the ratio of manganese component). The ternary mixed phase of $LiCoO_2$, $LiNiO_2$, and $LiMnO_2$,[30] $LiNi_{1/3}Co_{1/3}Mn_{1/3}O_2$,[31] has α-NaFeO2 structure[32] and alleviates the disadvantages[33] such as thermal instability of $LiCoO_2$ and $LiNiO_2$ and spinel-like phase transformation of LiMnO2 through less cation mixing which leads to an ultimate degradation of the performance. $LiNi_{1/3}Co_{1/3}Mn_{1/3}O_2$ containing Co^{3+}, Ni^{2+}, and Mn^{4+} shows a high reversible capacity and a good rate capability. In this respect, $LiNi_{1/3}Co_{1/3}Mn_{1/3}O_2$ is considered to be one of the most promising alternative materials for $LiCoO_2$. However, as I mentioned before, the component of transition metal and the ratio of transition metal are important to characterize the Ni-rich active material. So, to increase reversible capacity, the ratio of Ni increase in the Ni-rich materials. For example $LiNi_{0.6}Co_{0.2}Mn_{0.2}O_2$, $LiNi_{0.8}Co_{0.1}Mn_{0.1}O_2$[34], and $LiNi_xCo_yTM_{1-x-y}O_2$ (TM = Mn or Al, x>0.6, y≥0.1) have been studied. However, increasing the Ni content with a higher capacity in the active material is accompanied by poor structural, electrochemical and thermal stability.

Those Ni-rich cathode materials are usually synthesized by the reaction of a mixture of $M(OH)_2$ (M=Ni, Co, Mn) precursor and lithium hydroxide at a high temperature (600 − 1000 °C) under O_2 atmosphere. The $M(OH)_2$ (M=Ni, Co, Mn) precursor powders are synthesized uniformly and homogeneously by co-precipitation method.[35] The co-precipitation method can produce a uniform distribution of spherical particles. The synthetic method can produce a uniform distribution of spherical

powders with higher tap-density than non-spherical particles. The primary particles agglomerate together to form spherical secondary particles. The morphology and size of primary and secondary particles are controlled by several co-precipitation conditions such as temperature, reaction time, PH, etc.

Although, these Ni-rich cathode materials, $LiNi_xCo_yTM_{1-x-y}O_2$ (TM = Mn or Al)[36], have higher capacity than other cathode materials, they still need to improve their thermal, structural and electrochemically performance. Therefore some treatments are required for using the Ni-rich cathode materials.
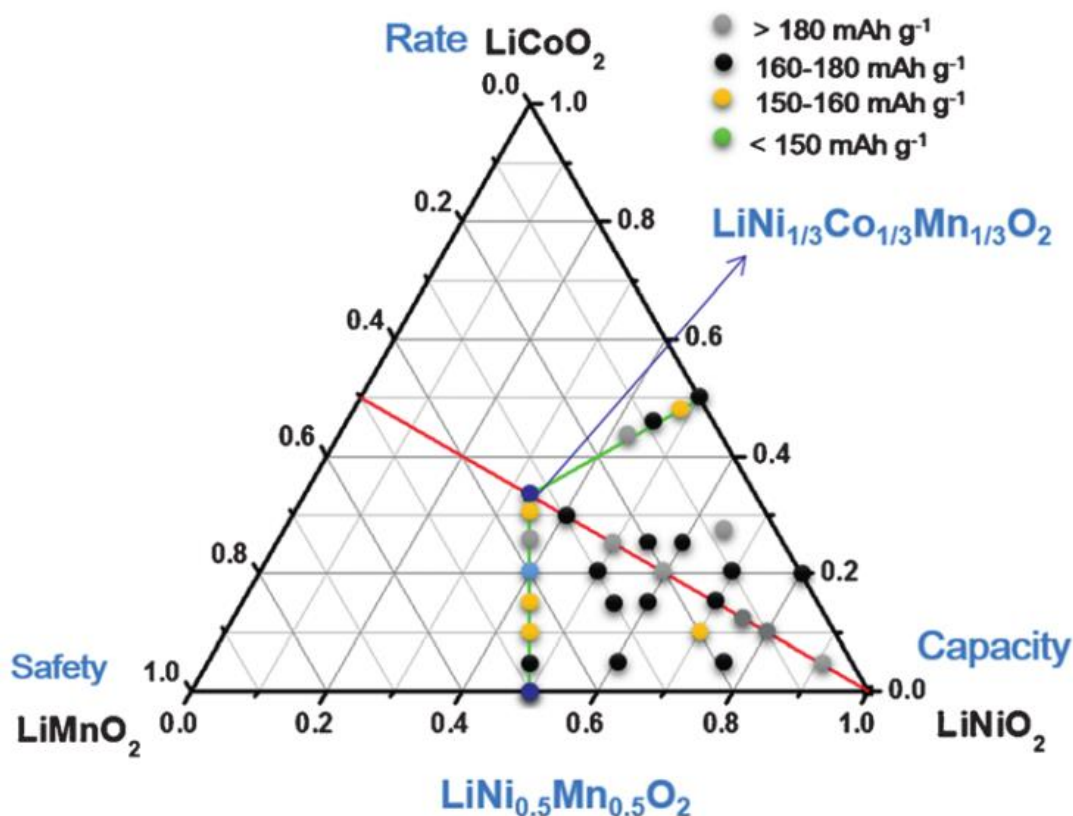
Figure 10. Compositional phase diagrams of $LiCoO_2$-$LiNiO_2$-$LiMnO_2$. The positions indicated by dots represent the described $LiNi_{1-x-y}Co_xMn_yO_2$ materials[16a].

Herein, I reported that highly stable $LiNi_{0.8}Co_{0.1}Mn_{0.1}O_2$ (that is, NCM) via a simple and one-step dry surface treatment approach (that is, G-NCM). The cobalt precursor was coated on the surface of the bare NCM in purpose to improve the material integrity by protecting the cathode surface against the acidic species attack. Furthermore, the transition metal (TM) concentration gradient in the primary particles ensured the structural stability by suppressing the evolution of micro-crack in the cathode particles and reducing transition metal dissolution. The more important thing is the enhanced material integrity allows stable and uniform solid electrolyte interphase (SEI) layer on the graphite anode, leading to unprecedented full-cell performance.

After the surface treatment, the high temperature (45 °C) cycle performance is improved from 20 % for bare NCM to 50 % for G-NCM. During the cycle, the G-NCM retains higher average coulombic efficiency of ~99.8 % than that of the bare NCM (~98.5 %). The electrochemical performance was prepared by full-cell. This finding could be a breakthrough for the LIB technology, providing a rational approach for the development of advanced cathode materials.

II. Experimental method

2.1 Introduction

The Ni-rich materials such as $LiNi_xCo_yMn_zO_2$ and $LiNi_xCo_yAl_zO_2$ are promising cathode materials. The Ni-rich materials have higher capacity than other material due to nickel ion, but their critical problems are also caused by the nickel ions. The biggest problem is phase transition which causes other various problems such as interruption of Li intercalation, increase resistance, oxygen evolution, etc. To prevent phase transition, simple dry surface treatment is suggested. The cobalt-rich phase on the surface of the cathode inhibited transition metal dissolution in the cathode and was enhanced structural stability. Also, through these effects, stable SEI layer was formed on the surface of the anode during charge and discharge process. So G-NCM sample had less cell resistance than that of NCM sample. In high temperature cycle test, bare NCM suffered from severe transition metal dissolution, crack in secondary particle, formation of thick and uneven SEI layer and some several side reaction. The formation of thick and uneven SEI layer interrupted lithium intercalation at graphite and disproportionate reaction formed lithium dendrite on the anode. On the contrary, in case of G-NCM sample, electrochemically inactive Co_3O_4 phase alleviated transition metal dissolution and phase transition of the cathode material. As a result, cycling performance and structural stability of cathode material was improved and stable SEI layer was formed on the anode.

2.2 Experimental method

Preparation of cathode materials

The $Ni_{0.8}Co_{0.1}Mn_{0.1}(OH)_2$ precursor was synthesized by co-precipitation. Nickel sulfate, cobalt sulfate and manganese sulfate are mixed with a molar ratio of Ni : Co : Mn = 8 : 1 : 1 and diluted with a concentration of 2.0mol/L in distilled water. The precipitation occurs in a CSTR (continuous stirred tank reactor) under N_2 atmosphere with 2.0mol/L NaOH solution and NH_4OH solution as a chelating agent were separately fed into the CSTR at 50°C. The PH value was controlled around 11. The precursor and $LiOH \cdot H_2O$ (Li : M = 1.02 : 1) were mixed and annealed at 780°C for 20h under O_2 atmosphere in RHK (Roller Hearth Kiln). The final product is $LiNi_{0.8}Co_{0.1}Mn_{0.1}O_2$ (bare NCM). The surfaced treated NCM (G-NCM) was synthesized by the dry process. 30g of the NCM powder and 1.05g of cobalt precursor were simply mixed by Thinky mixer for 3 minutes at 2000rpm. The mixed power was calcinated over 500°C under O_2 atmosphere.
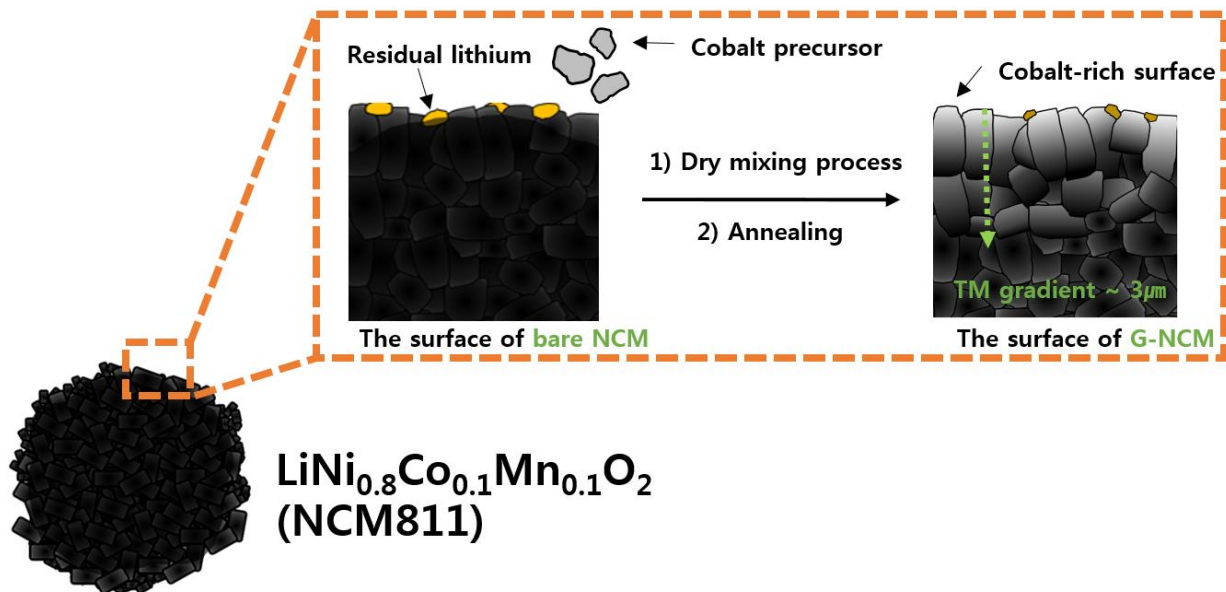

Figure 11. Schematic view of G treatment on $LiNi_{0.8}Co_{0.1}Mn_{0.1}O_2$.

Electrochemical properties

The electrochemical properties were tested in both coin-type 2032R cell which contains a cathode electrode and lithium metal as counter electrode and pouch-type full cell. The cathode slurry was consisted of 96 wt% of active material, 2 wt% of Super-P carbon black, and 2 wt% of poly(vinylidene fluoride) (PVDF) binder in *N-methyl-2-pyrrolidinine* and coated on Aluminum current collector with slurry loadings of 10.2 mg/cm^2 and loading density is 3.0 g/cc. The anode slurry was consist of 96 wt% of active material(S360MB), 1 wt% of Super-P carbon black, 1.5 wt% of Styrene-Butadiene Rubber (SBR) and 1.5 wt% of carboxymethyl cellulose (CMC) solution in distilled water and coated on Copper current collector with 6.8 mg/cm^2 and loading density is 1.45 g/cc. After casting, both cathode and anode electrode are dried at 110 ℃ in a vacuum.

The coin-type 2032R half-cell was assembled in a dry argon-filled glove box. The electrolyte was 1.0 M LiPF$_6$ with a mixture of EC and EMC (1:2 vol%). The galvanostatic charge-discharge cycling test of the half-cell was performed in a voltage range from 3.0 V to 4.3 V (vs Li/Li$^+$) at a 0.5 C charge rate and a 1 C discharge rate. Before electrochemical tests, the cell was galvanostatically charged to 4.3 V at 0.1 C rate, and maintained at 4.3 V until the current decreased to 0.05 C rate, then discharged to 3.0 V (vs Li/Li$^+$). The pouch-type full cell was assembled in dry room. The charge N/P ratio was 1.05 and discharge N/P ratio was 1.14. The electrolyte was 1.05 M LiPF$_6$ in a mixture of EC, EMC and DEC (30:60:10 vol%) with 1 wt% of Vinylene carbonate (VC) and 0.5 wt% of Polysulfone which is injected 0.3 cc in the each pouch-cell. The size of the cathode is 5 cm^2, anode is 5.94 cm^2, and separator is 7.8 cm^2. Galvanostatic charge and discharge test was performed between 3.0 V and 4.2 V (vs Li/Li$^+$). Before electrochemical tests, the cell was galvanostatically charged to 4.2 V at 0.1 C rate, and maintained at 4.3 V until the current decreased to 0.05 C rate, then discharged to 2.8 V (vs Li/Li$^+$).
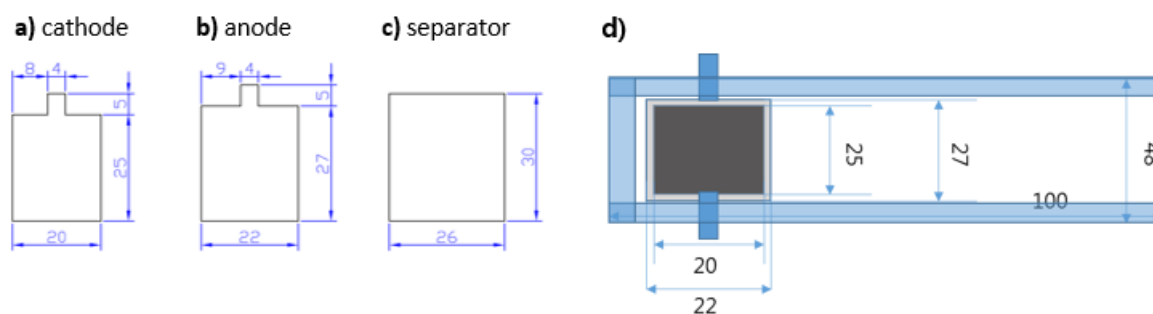
Figure 12. Pouch type full cell design. The standard of **a)** cathode electrode is 20.0 mm x 25.0 mm and that of **b)** anode is 22.0 mm x 27.0 mm. **c)** Separator size is 26.0 mm x 30.0 mm. **d)** The whole pouch size is 48.0 mm x 100.0 mm.

Instrumental analysis

The crystalline phase of samples was identified by powder X-ray diffractometer (XRD, D/Max2000, Rigaku) using Cu-Kα radiation. The morphology and atomic-scale observation of powders was examined by scanning electron microscopy (SEM, S-4800, HITACHI) and high resolution-transmission electron microscopy (HR-TEM, JEM-2100F, JEOL). TEM samples were prepared by focused ion beam (FIB, JEM-2100F, JEOL). The HAADF-STEM images were taken using a probe-side aberration corrected TEM ((JEOL JEM-2100F). The energy dispersive X-ray spectroscopy (EDX) analysis was conducted using dodeca-pole aberration corrected TEM (JEM-ARM300F, JEOL). Time-of-flight secondary mass ion spectroscopy (ToF-SIMS, TOF SIMS5, ION TOF) was used to investigate transition metal dissolution and by-product from side reaction with electrolyte.

III. Results and Discussion

3.1 Morphology and Surface Composition

Figure 13 shows a scanning electron microscope (SEM) image and cross-sectional scanning transmission electron microscope (STEM) image of a NCM and G-NCM secondary particle. Both NCM and G-NCM shows similar spherical morphology that the primary particles agglomerate together to form large secondary clusters. The surface of G-NCM is covered with small coating particles (~50 nm).

Table 1 shows physical and chemical properties of NCM and G-NCM. The secondary particle size of NCM and G-NCM is approximately 11~12 μm. Two samples have similar Tap density and Pallet density. BET data shows the surface area of the G-NCM (0.51 m^2/g) is three times higher than the NCM (0.18 m^2/g). The amount of free lithium (included both Li$_2$CO$_3$ and LiOH) which is related to side reaction and gas evolution in G-NCM (0.15 wt%) decreases in comparison with NCM (0.19 wt%).

Powder X-ray diffraction (XRD) patterns of NCM and G-NCM in Figure 14a) indicate dry surface treatment doesn't affect layered structure of G-NCM. All peaks of samples were well exhibited a single phase of layered structure without any impurity.

Transmission Electron Microscope (TEM) data shows there are no particle size and morphology difference between NCM and G-NCM. Also, the thickness of cation mixing layer on NCM and G-NCM surface before electrochemical test are almost same (~3 nm).
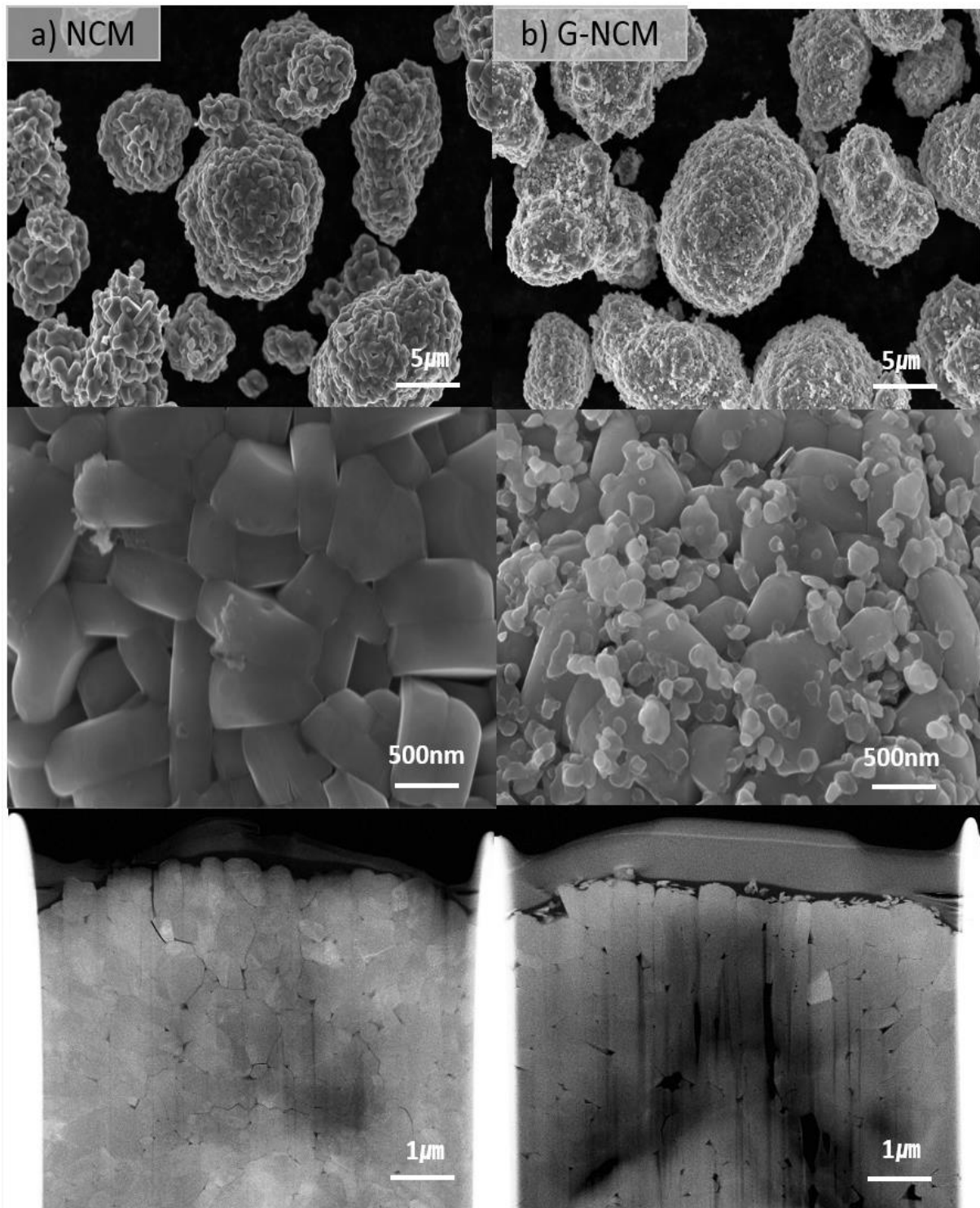
Figure 13. SEM and STEM images of a) $LiNi_{0.8}Co_{0.1}Mn_{0.1}O_2$ and b) surface treated $LiNi_{0.8}Co_{0.1}Mn_{0.1}O_2$ (G-NCM).

Table 1. Physical properties of NCM and G-NCM.

Lot no.	NCM	G-NCM
D50 [μm]	12.36	11.32
TD [g/cc]	2.44	2.58
PD [g/cc]	3.46	3.45
BET	0.18	0.51
Moisture [ppm]	359.6	376.2
Li_2CO_3 / LiOH	0.483 / 0.355	0.385 / 0.271
Total free Li [wt%]	0.19	0.15
PH	11.80	11.78
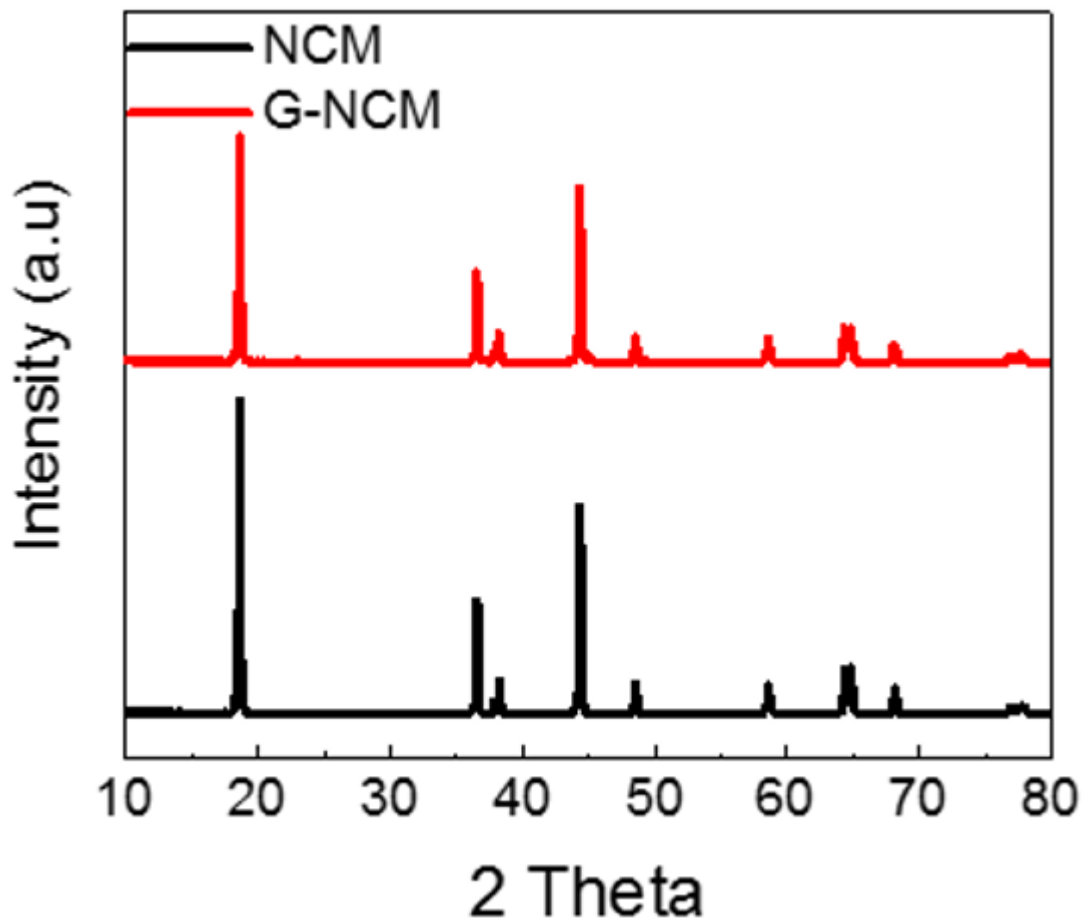
Figure 14. Powder X-ray diffraction (XRD) patterns of NCM and G-NCM.
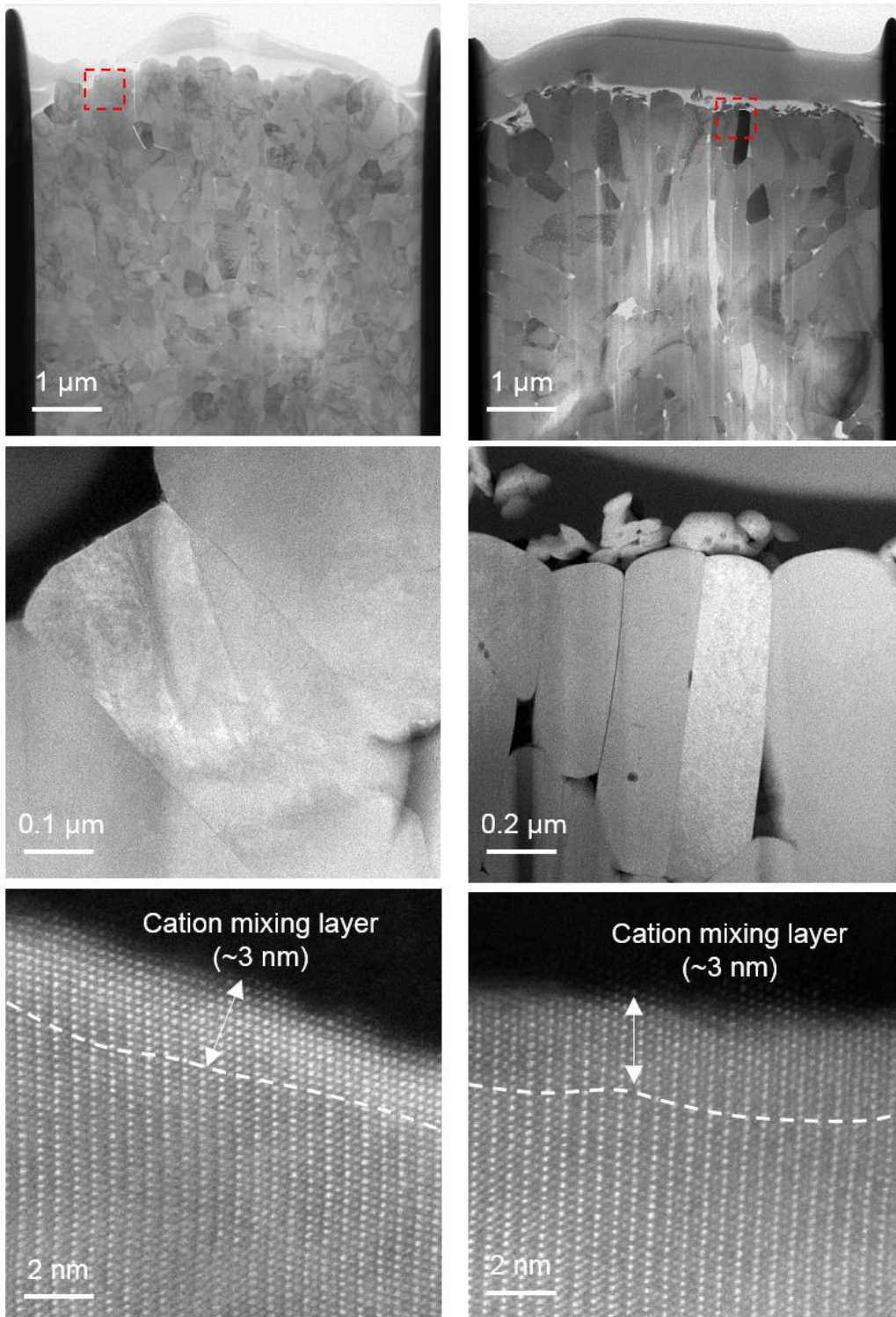
Figure 15. TEM images of a) NCM and b) G-NCM. NCM and G-NCM have similar thickness of cation mixing layer (~3 nm)**.**

To analyze coating layer after G-treatment, TEM and EDS measurement are performed. Figure 16 a) and Figure 16 b) shows spherical particles which are regarded as coating layer are distributed on the surface of G-NCM particle. Figure 16 c) STEM image indicates the coating layer is composed of three phase (one layered phase and two kinds of spinel phase). The thickness of spinel phase is about 2~3 nm. Two kinds of spinel phases are marked red line and blue line respectively and Figure 16 d) shows the red one is Co_3O_4 phase which is full of cobalt ion and blue one is $Li_xCo_2O_4$ spinel structure ($x < 1$).

To investigate the composition of coating layer, EDS measurement was performed. The coating layer is compose of cobalt-rich phase (the ratio of cobalt is above 50 %). Also, the ratio of Ni is under 1 %. It means small particles located on surface of G-NCM is not a fragment of G-NCM but foreign coating material. The EDS data is evidence for the red one which is located in surface of the coating layer is Co_3O_4 phase and the blue one is $Li_xCo_2O_4$ spinel structure and inner part of coating layer is cobalt-rich layered structure. Co_3O_4 spinel structure which is located on the particle is electrochemically inactive phase. Therefore it keeps stable structure during charge and discharge process. As a result coating layer (included electrochemically inactive phase) prevents transition metal dissolution.

Figure 18 b) shows transition metal gradient on primary particle of G-NCM. The depth of TM gradient is about 60 nm. The surface of primary particle which is located on the surface of secondary particle shows higher cobalt concentration than the cobalt concentration of bare NCM, 10 % (> 20 %). Coating substance permeates an inner primary particle which is located 3 μm above the surface of secondary particle. It means coating effect affect not only surface primary particle but also inner primary particles.
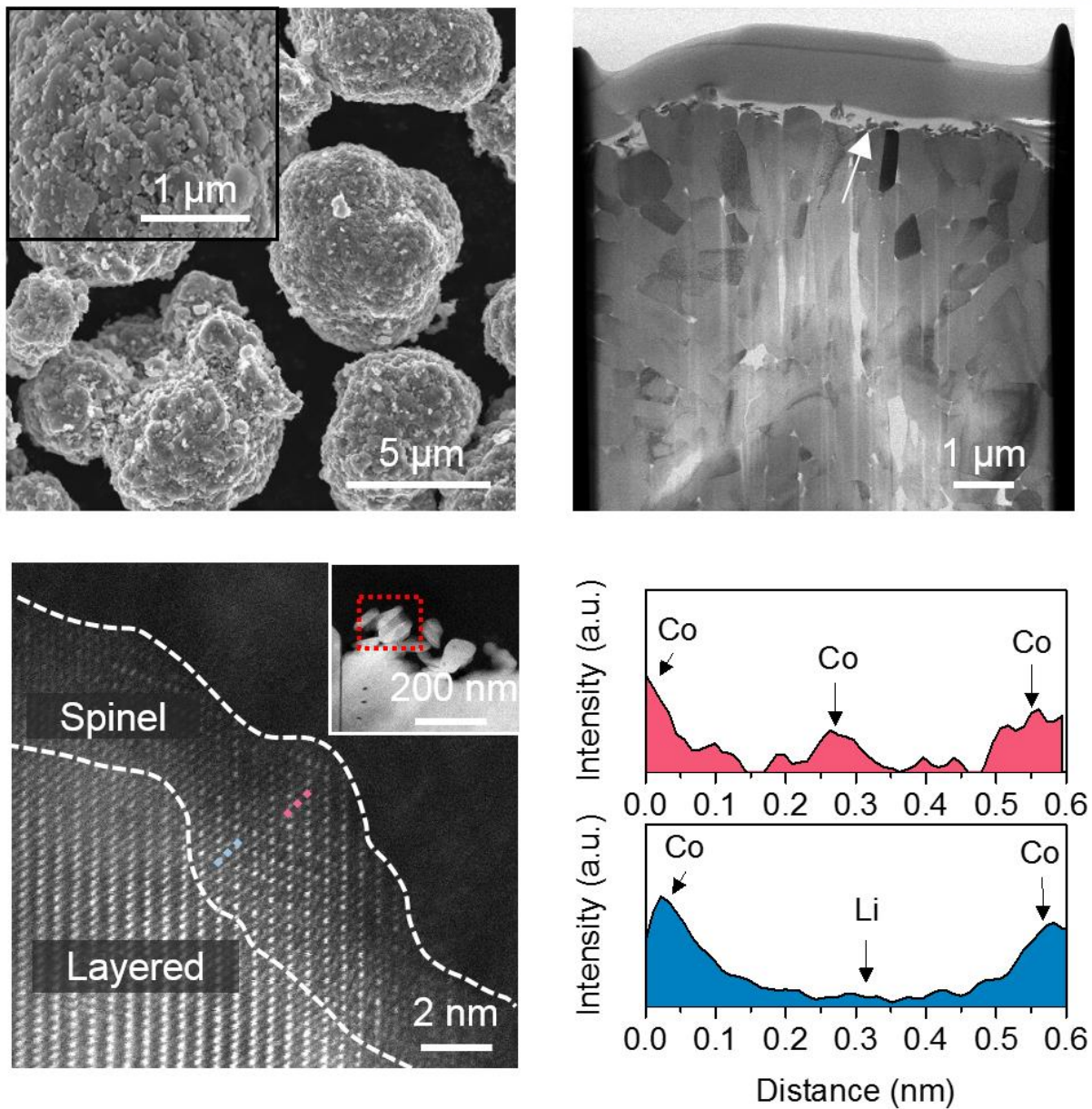
Figure 16. a) SEM image of G-NCM. **b)** FIB image of G-NCM. An arrow indicates coating layer. **c)** coating layer consist of three cobalt rich phase (one layered phase and two kinds of spinel phase) **d)** two different spinel phase. The red one is Co_3O_4 and the blue one is $Li_xCo_2O_4$ (x < 1).
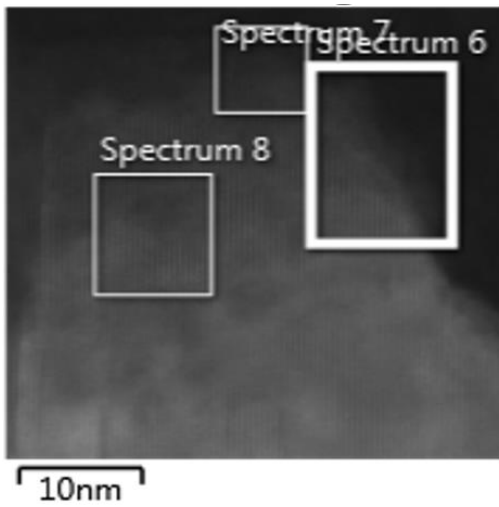
Spectrum	Ni (wt%)	Co (wt%)	O (wt%)
6	1.33	57.99	40.68
7	0	49.07	50.93
8	0.81	60.89	38.31

Figure 17. TEM image of coating material.
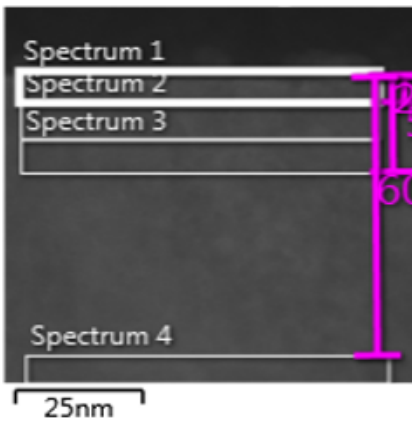
Spectrum	Ni (wt%)	Co (wt%)	Mn (wt%)
1	77.16	11.69	11.15
2	78.47	10.02	11.51
3	78.02	12.98	9
4	79.36	10.91	9.73
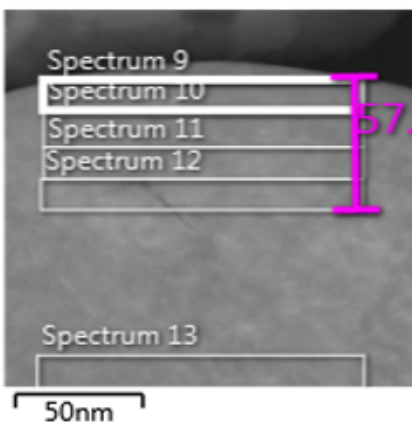
Spectrum	Ni (wt%)	Co (wt%)	Mn (wt%)
9	64.36	25.27	10.37
10	74.37	15.65	9.99
11	78.42	11.68	9.90
12	80.49	10.94	8.57
13	80.70	10.80	8.49

Figure 18. TEM and EDS images of a) NCM and b) G-NCM**.**

3.2 Electrochemical results

3.2.1 Half-cell results

The electrochemical properties of each sample were evaluated using coin-type 2032R lithium half-cells. Figure 19 shows the formation graph of the NCM and G-NCM at room temperature (25 ℃). Coin-type half cells were charged at 0.1 C rate (1 C = 200 mA g^{-1}) to 4.3 V and maintained at 4.3 V until the current decreased to 0.05C rates, then discharged at 0.1 C rate to 3.0 V at 25 ℃. The first discharge capacity of G-NCM is 198 mAh g^{-1}. It is higher than the NCM (193 mAg $^{-1}$). The G-NCM sample shows higher capacity retention of 59 % after 200 cycles (from 183 to 108 mAh g^{-1}) than the NCM sample (53 % retention from 182 to 97 mAh g^{-1}) at room temperature and also higher capacity retention of 58 % after 150 cycles (from 215 to 124 mAh g^{-1}) than the NCM sample (23 % retention from 207 to 48 mAh g^{-1}). Figure 20 b) and 20 d) exhibits charge and discharge voltage profiles of NCM and G-NCM with increasing cycle number at 25 ℃ and 45 ℃, respectively. The G-treatment is more effective at high temperature than room temperature, Because TM dissolution is more severe at high temperature than room temperature. Dissolved TM increases side reactions and produces by-products at the anode side. Furthermore, the capacity of G-NCM from constant voltage mode was much lower than that of NCM. The capacity from constant voltage mode is correlated with the overpotential. It means the G-NCM has lower overpotential than NCM one.
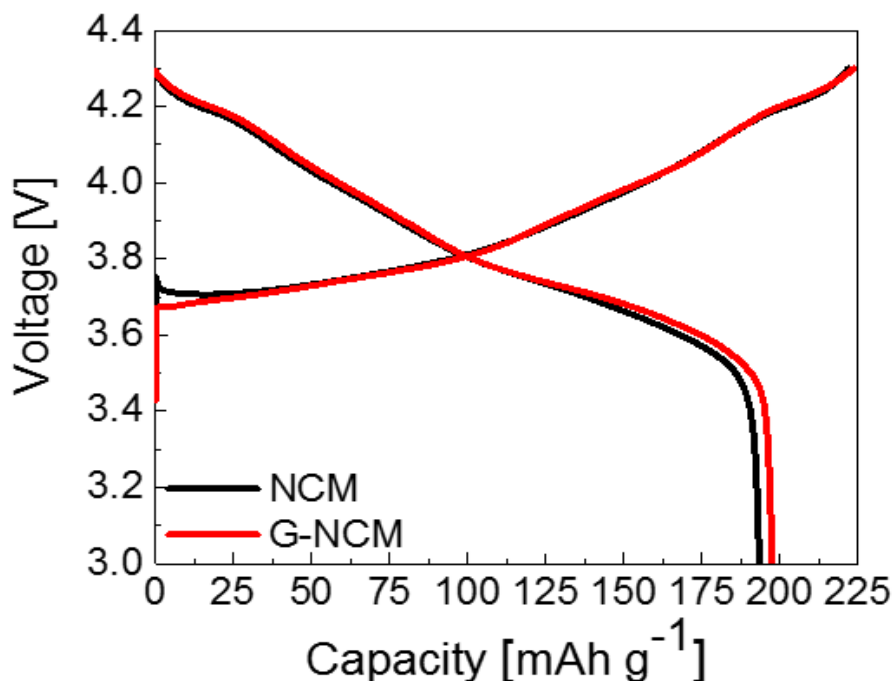
Figure 19. The formation graph of NCM and G-NCM, respectively, where the operating voltage ranged from 3.0-4.3 V (C-rate : 0.1 C).
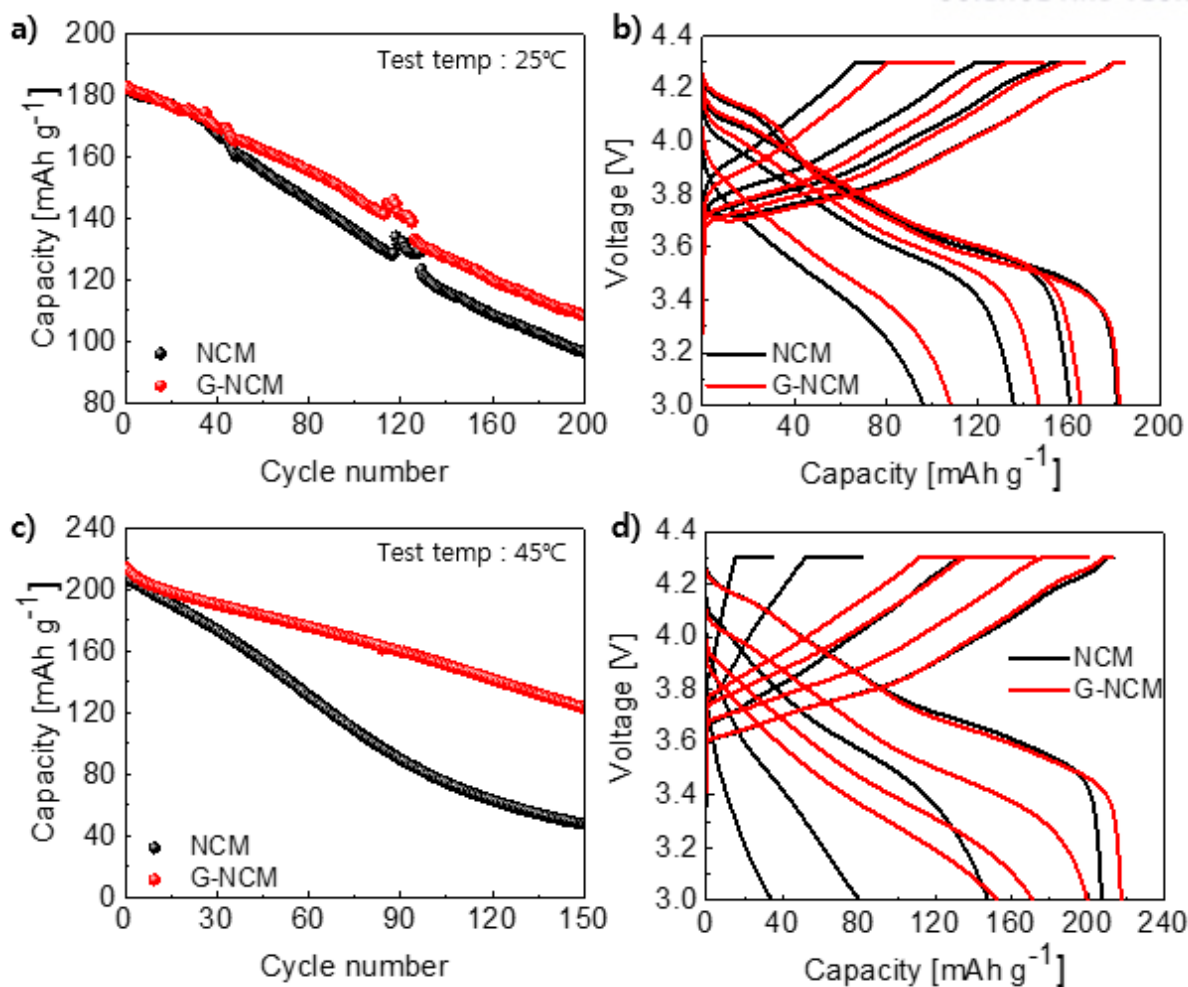
Figure 20. Electrochemical characterization of the NCM and G-NCM **a)** Room temperature (25 °C) cycling performance of the NCM and G-NCM (charge and discharge C-rate: 0.5 C and 1 C) **b)** Voltage profiles of the NCM and G-NCM from RT cycle test at 1st, 50th, 100th and 200th.**c)** High-temperature (45 °C) cycling performance (charge and discharge C-rate: 0.5 C and 1 C) **d)** Voltage profiles of the NCM and G-NCM from HT cycle test at 1st, 50th, 100th and 150th.

3.2.2 Full-cell results

The pouch-type full cell data shows a similar tendency to half-cell data. The anode is called S360MB. Its reversible capacity is 340 mAh g^{-1} and efficiency was 94 %. Table 4 shows calculated capacity of full-cell charge N/P ration is 1.05 and discharge N/P ratio of 1.14. The expected charge capacity is 11.9 mAh and discharge capacity is 10.3 mAh. The designed full cell scheme is in Figure 12 The standard of cathode electrode is 20.0 mm x 25.0 mm and that of anode is 22.0 mm x 27.0 mm. Separator size is 26.0 mm x 30.0 mm. The whole pouch size is 48.0 mm x 100.0 mm.

The first cycle charge and discharge voltage profiles of NCM and G-NCM full cells are shown in figure 21. The full-cell was charged at 0.1 C rate (1 C = 10 mAh) until reached to 4.2 V and maintained at the voltage till current decreased to 0.02 C rate, then discharged at 0.1 C rate to 2.8 V at 25 °C. The discharge capacity of NCM and G-NCM is were 11 and 10 mAh and the coulombic efficiency of NCM and G-NCM were 89 and 88, respectively. Also, in table 6, DC-IR results which are measured after formation process shows similar resistance values. There are no remarkable difference in the first charge and discharge cycle. Figure 22 shows the results of cycle test of NCM and G-NCM samples. The results of cycle test are similar to half-cell data. The G-NCM sample shows higher capacity retention of 84 % after 400 cycles (from 9.8 to 8.2 mAh) than the NCM sample (62 % retention, from 9.6 to 6.0 mAh) at room temperature and also higher capacity retention of 50 % after 500 cycles (from 8.8 to 4.4 mAh) than the NCM sample (21 % retention, from 8.6 to 1.8 mAh). The voltage profiles of NCM and G-NCM show that the average working voltage of the NCM is much higher than that of G-NCM during charging.

Table 2. Calculated capacity of full cell (charge N/P ratio : 1.05 discharge N/P ratio : 1.14 operating voltage :2.8-4.2 V).

Sample	1st Charge capacity [mAh]	1st Discharge capacity [mAh]	Retention [%]
NCM, G-NCM/ S360-MB	11.9	10.3	88.5

Figure 21. Formation graph of NCM and G-NCM, where the operating voltage ranged from 2.8-4.2 V.

Table 3. Initial charge and discharge capacity of NCM and G-NCM with columbic efficiency.
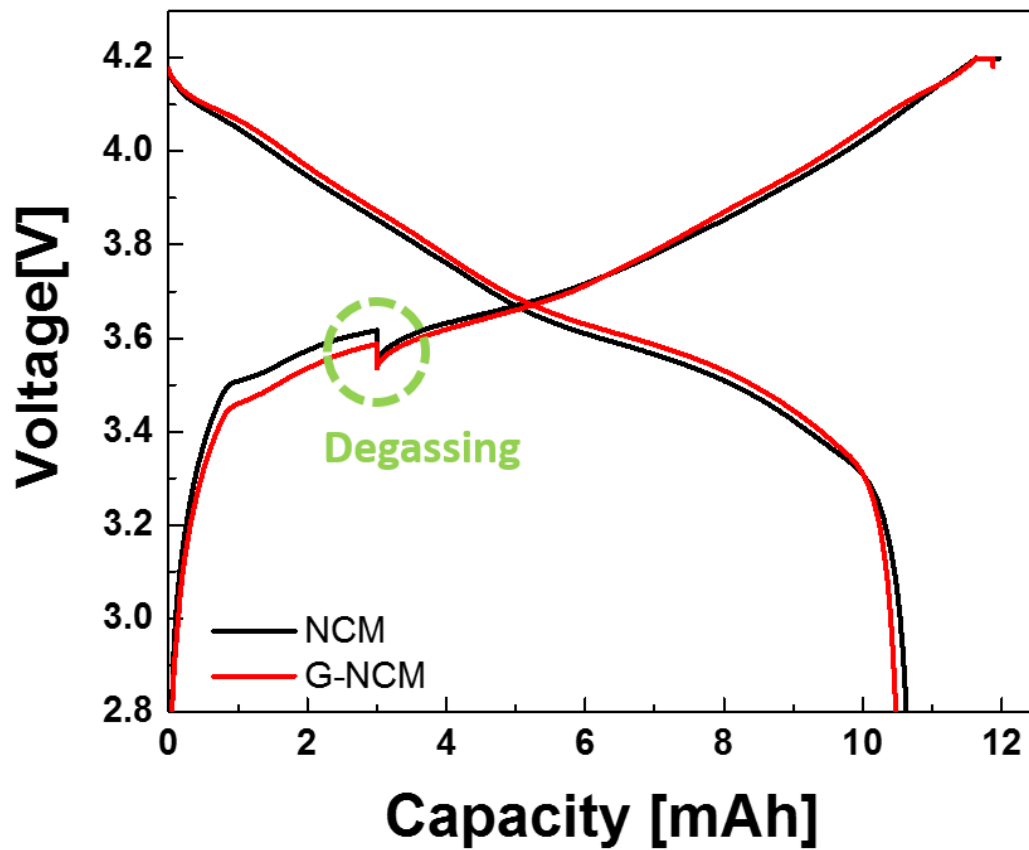
Sample	1st Charge capacity (mAh)	1st Discharge capacity (mAh)	C.E (%)
NCM	11.96	10.63	88.9
G-NCM	11.88	10.47	88.2

Table 4. DC-IR data of NCM and G-NCM.

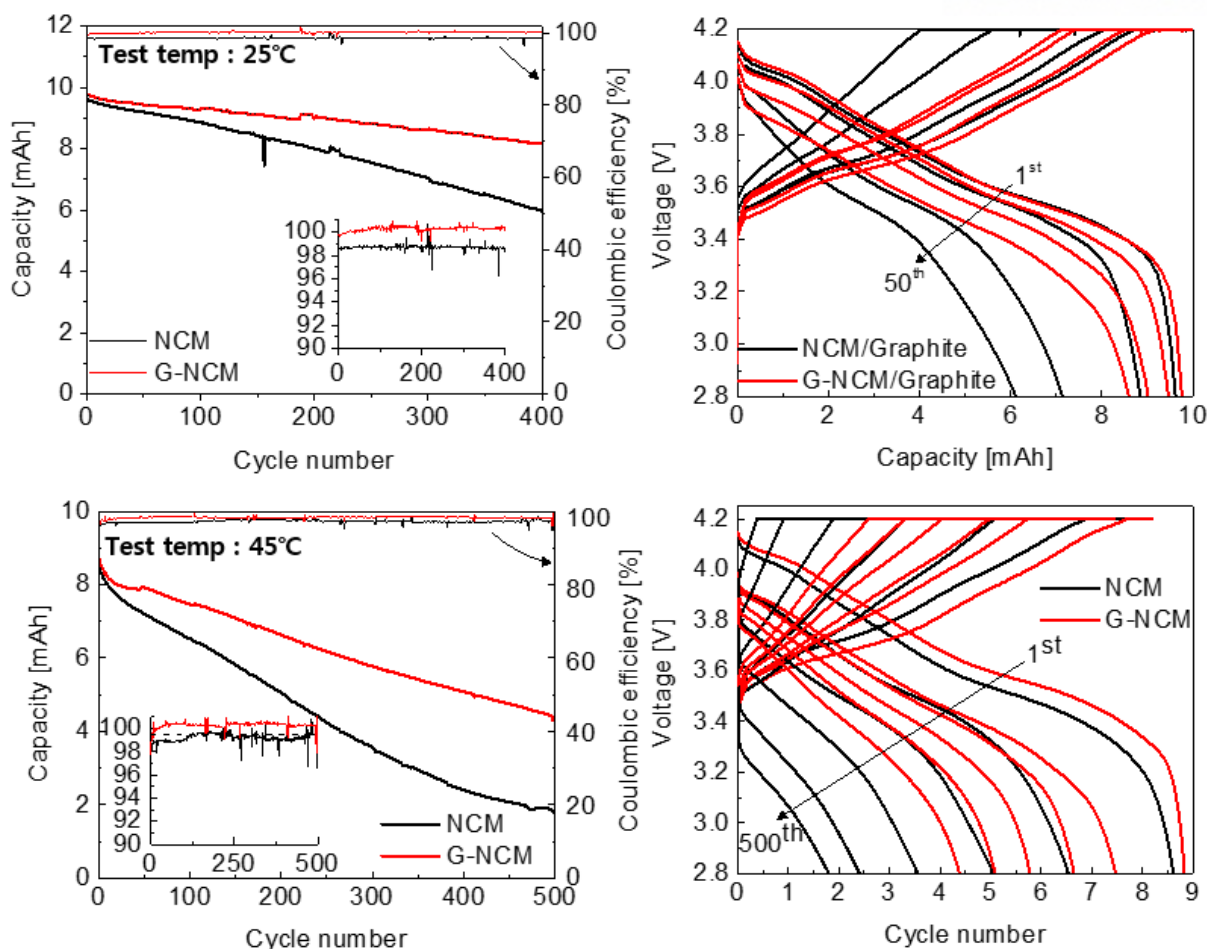| Sample	R_{charge} (Ω)	$R_{discharge}$ (Ω)
NCM	4.52	4.10
G-NCM	4.30	4.06

Figure 22. Electrochemical characterization of the NCM and G-NCM full-cell **a)** Room temperature (25 °C) cycling performance of the NCM and G-NCM (charge and discharge C-rate: 0.5 C and 1 C) inner graph means columbic efficiency of each cycle. **b)** Voltage profiles of the NCM and G-NCM from RT cycle test at 1st, 100th, 300th and 400th. **c)** High-temperature (45 °C) cycling performance (charge and discharge C-rate: 0.5 C and 1 C) **d)** Voltage profiles of the NCM and G-NCM from HT cycle test at 1st, 100th, 200th, 300th, 400th and 500th.

3.3 Structural analysis

3.3.1 Cathode

To conform the effects of G-treatment, various analyses were performed. After 500th cycle test at 45 °C, the NCM and G-NCM were disassembled to analysis. Figure 23 a) and b) show the cross-sectional SEM images of NCM electrode and G-NCM electrode before cycle test and after cycle test, respectively. Before 45 °C cycle test, both NCM sample and G-NCM sample had a little crack only on the surface side of electrode. Inner secondary particles which were close to current collector kept their own shapes. After cycle test, the NCM sample had severe micro-cracks along the grains, but micro-cracks was visibly decreased in the G-NCM sample. The micro-cracks of the secondary particle extended the contact area with electrolyte. As a result, the cathode material undergoes TM dissolution and side reactions, accelerating structural degradation.

In well-ordered layered phase, the Li slab cannot be detected as white dots in HR-TEM images. However, Ni^{2+} ions which have similar ionic radius with Li^+ ion easily move into Li slab, and white spots can be detected for such materials. This is cation mixing and common in Ni-rich cathode materials. Cation mixing is identified as a hexagonal white spots with [200] and [111] plans that indicates of NiO rock-salt phase. Figure 24 shows HR-TEM images of the a) NCM and b) G-NCM particles along the [110] zone axis and FFT images (Randomly selected NCM and G-NCM particle). Before cycling, both the NCM and G-NCM had only 3nm scale cation mixing layer on the surface of primary particle. Inner part of both materials was layered phase (in Figure 15). After cycling, cation mixing layer widen both NCM and G-NCM. The thickness of cation mixing layer of the NCM (~40 nm) is thicker than the G-NCM (~10 nm). The phase transition in the cathode material became severe by reaction between the grain and electrolyte. Many micro-cracks in the NCM samples (in Figure 23) increased side reaction due to their active sites.
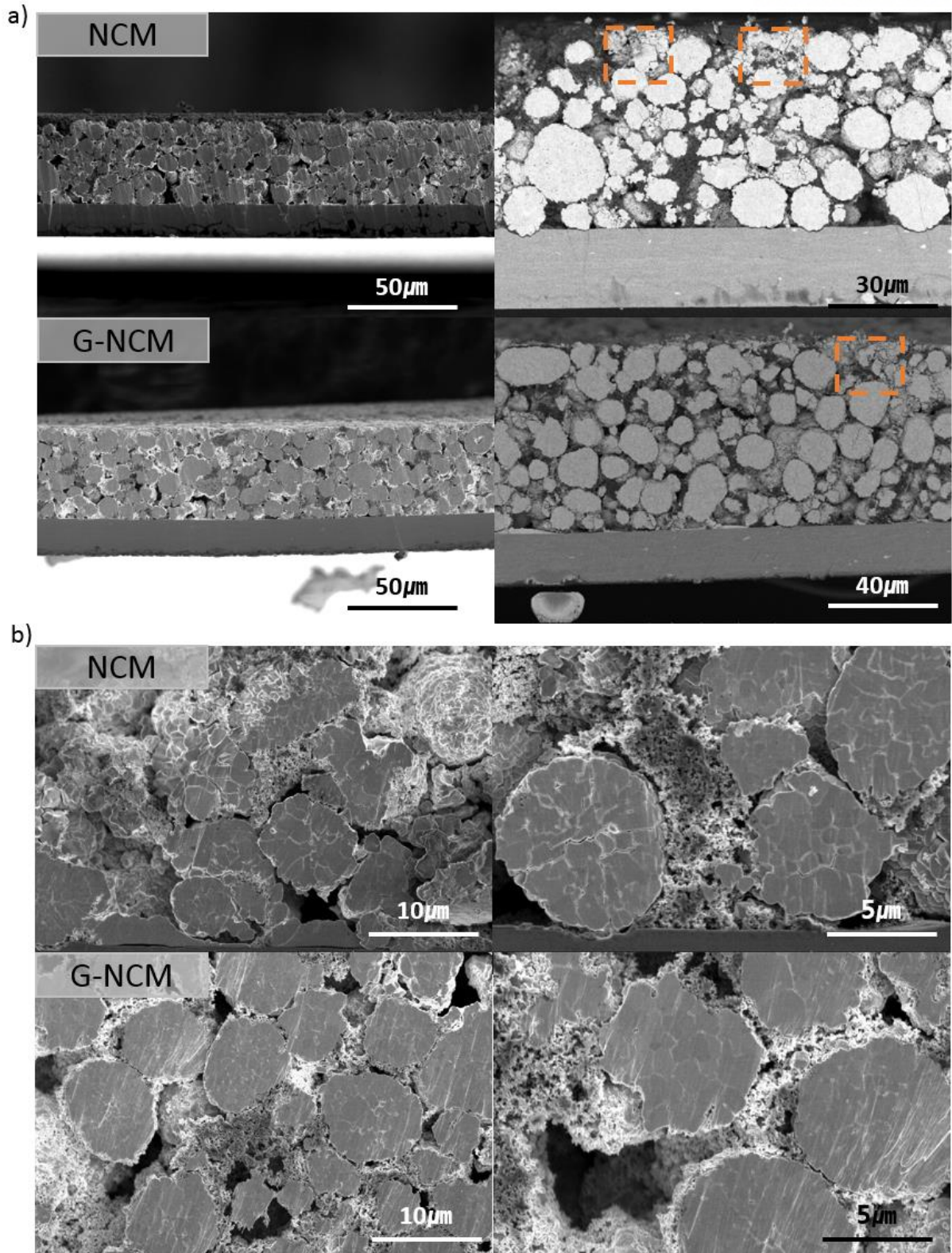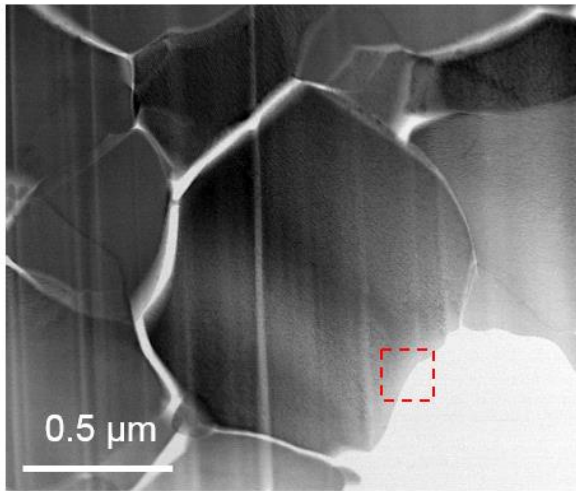
Figure 23. The cross-sectional SEM images of NCM electrode and G-NCM electrode. **a)** Before and **b)** after 500 cycles at 45 ºC.

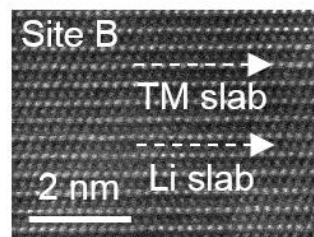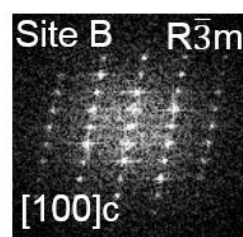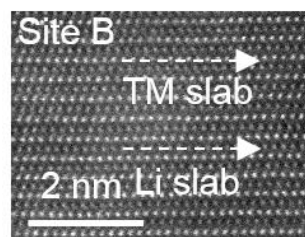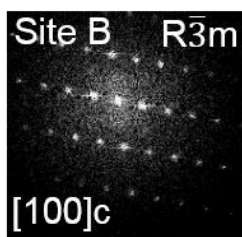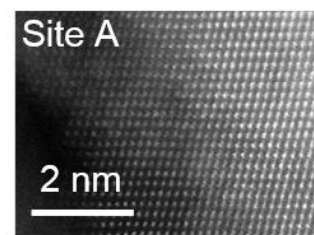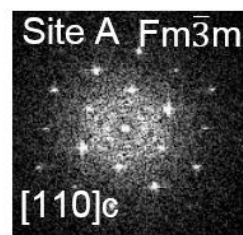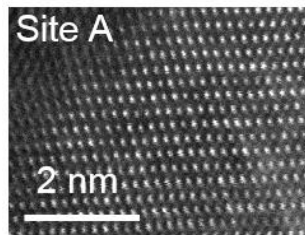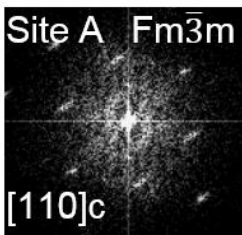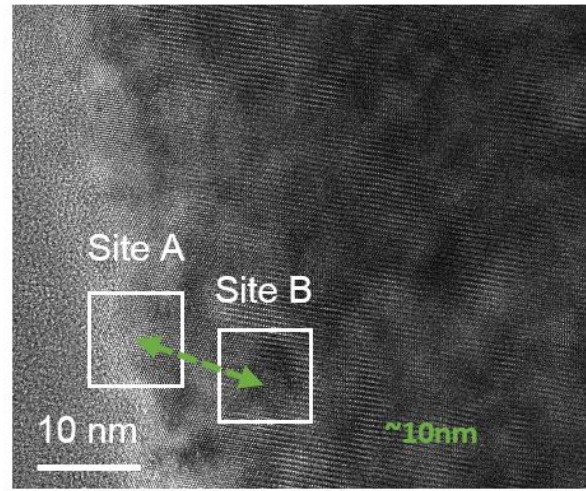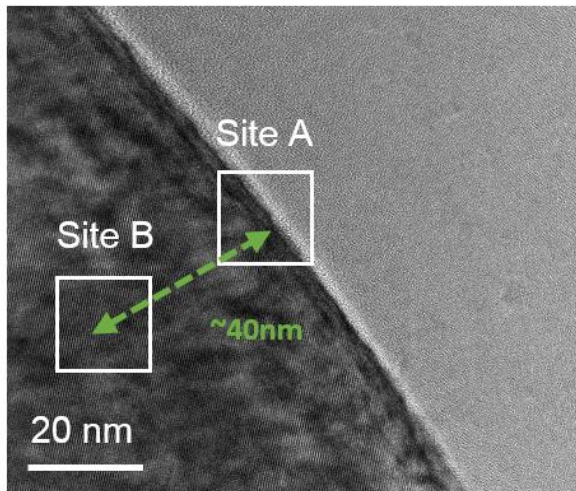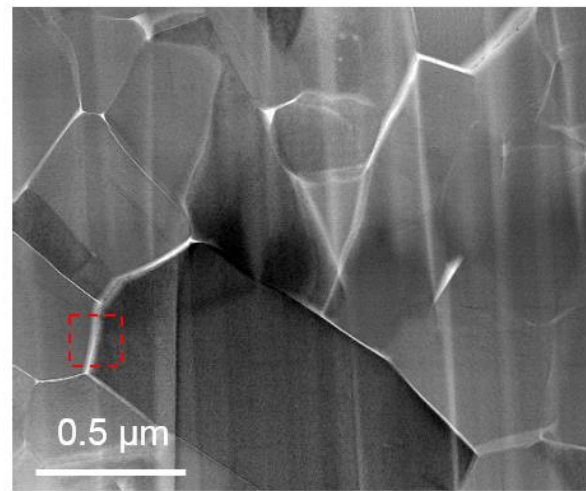**Figure 24.** HR-TEM images of **a)** NCM and **b)** G-NCM after 500 cycles at 45 °C.

To investigate the degree of transition metal (TM) dissolution, EDS scanning and TOF-SIMS (Time of Flight - Secondary Mass Spectrometry) were carried out. Figure 25 shows TEM images of primary particle and EDS scanning result of the NCM and G-NCM which are corresponding to TEM images. The EDS scanning was carried out from the outside of the primary particle to the inside. The start point and the end point of scanning is marked by a white arrow at TEM images. The outside space, commonly called as a grain, is empty space. However, EDS scanning data of NCM indicates TM was founded on the outside of primary particle and TM deficient region was formed on the surface of NCM (~10 nm). That is transition metal ions at the surface were dissolved in electrolyte.
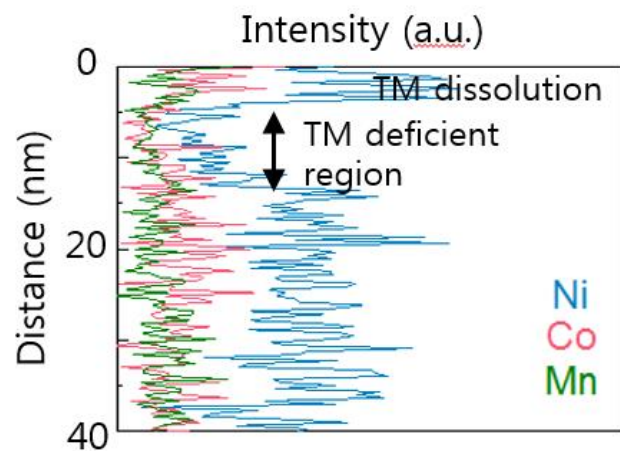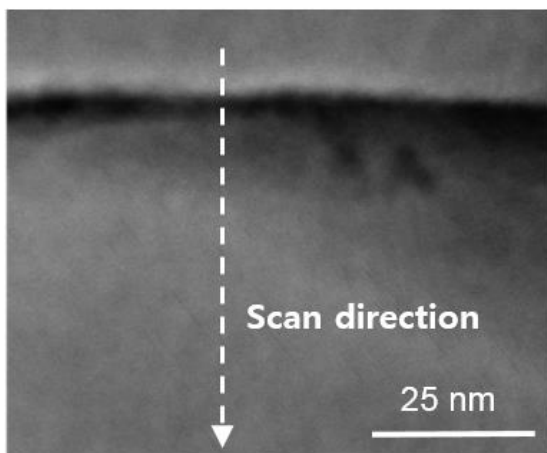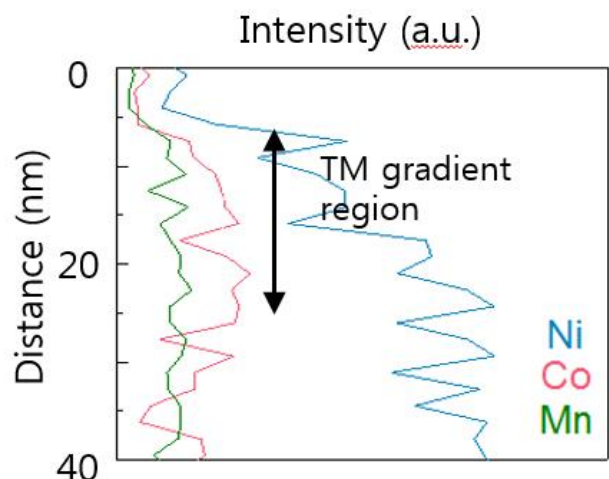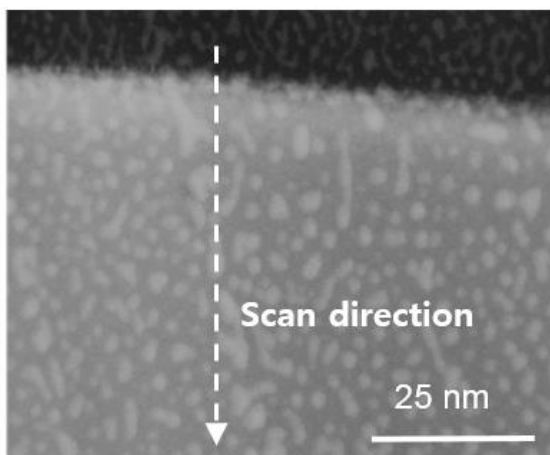
Figure 25. TEM image and EDS scanning images of **a)** NCM and **b)** G-NCM.

Another evidence for TM dissolution is TOF-SIMs results of the anode samples. TM ions which were produced from the cathode material were dissolved in electrolyte. Some TM ions were accumulated to the surface of the anode during cycling test. In Figure 26, the graphite which is matched with NCM had high concentration of Ni and Co ion than that of G-NCM. Dissolved TM ions can affect both the cathode material and the anode electrode. Decreased redox center in cathode material causes capacity fading. Furthermore, accumulation of TM ions at the anode causes unnecessary redox reaction and increase resistance.
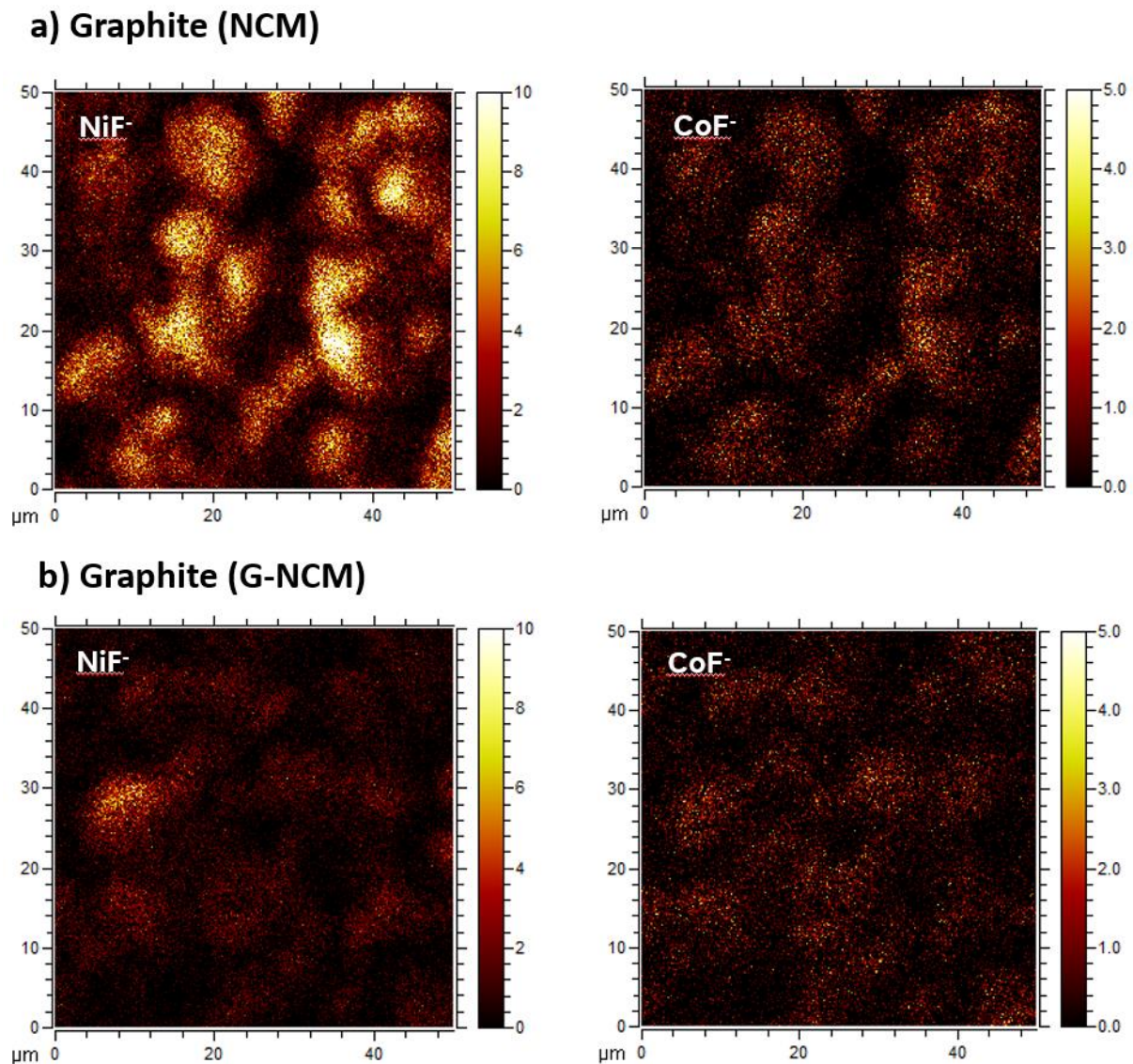
Figure 26. TOF-SIMS images of **a)** NCM and **b)** G-NCM.

3.3.2 Anode

Figure 27 shows SEM and EDS images of graphite. In figure 27 a), the surface of the graphite which was coupled with NCM was unclean. The small particles were on the surface. By contrast, the surface of the graphite with G-NCM was clean. The cross-sectional SEM images and EDS shows SEI layer on the graphite (NCM sample) was not uniform and very thick. For more accurate analysis, TEM and EDS analysis were carried out. The TEM and ESD results were well matched with SEM results. The SEI layer of NCM/graphite sample was uneven, thick and dissolved transition metals were contained in SEI layer. Moreover, the EDS results of NCM/graphite sample indicated excessive Ni was agglomerated in graphite.

After the disassembly of the full-cell, the surface of the anode of NCM/graphite sample changed color due to Li dendrite and Li dendrite was confirmed by SEM images. (In Figure 29 a) and b)). The changed color of the anode was easily seen with the naked eye and distinguished from G-NCM/graphite sample. For more accurate analysis of Li dendrite and material on the anode, ToF-SIMS depth profiling was carried out. (In Figure 29 c) and d)). As sputter times increases, the depth of sample from the surface to inside increases. Dissolved Ni ions were appeared at the surface of graphite both NCM and G-NCM samples. These results reminded transition metal dissolution of samples. The blue peak of Li ion in Figure 30 d) indicated similar tendency to P and F ions and was expected to SEI layer which was formed on the surface of the anode. Through the intensity of the P and F elements over sputter tome, we can predict the thickness of SEI layer of NCM/graphite sample was larger than that of G-NCM/graphite sample. The sharp peak in Figure 30 d) indicated thin SEL layer while the broad peak in Figure 30 c) indicated thick SEI layer. The Li peak in Figure 30 c) was separated with P and F element and expected as Li dendrite.

a) Graphite (NCM)
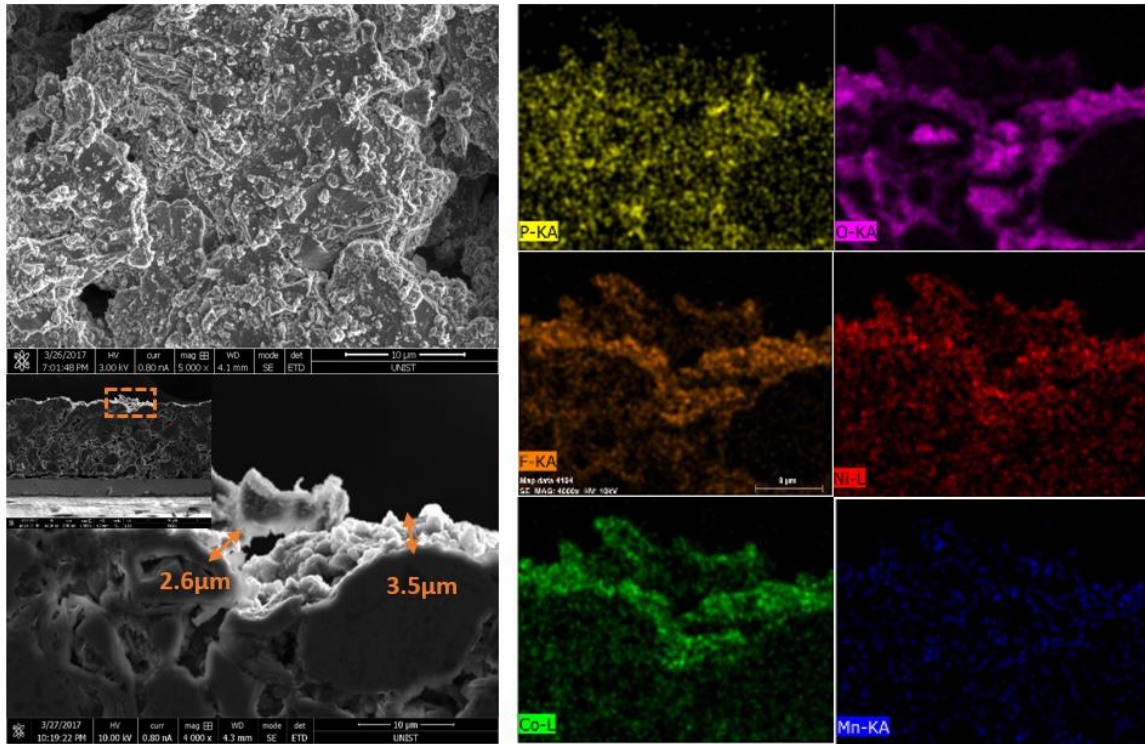
b) Graphite (G-NCM)
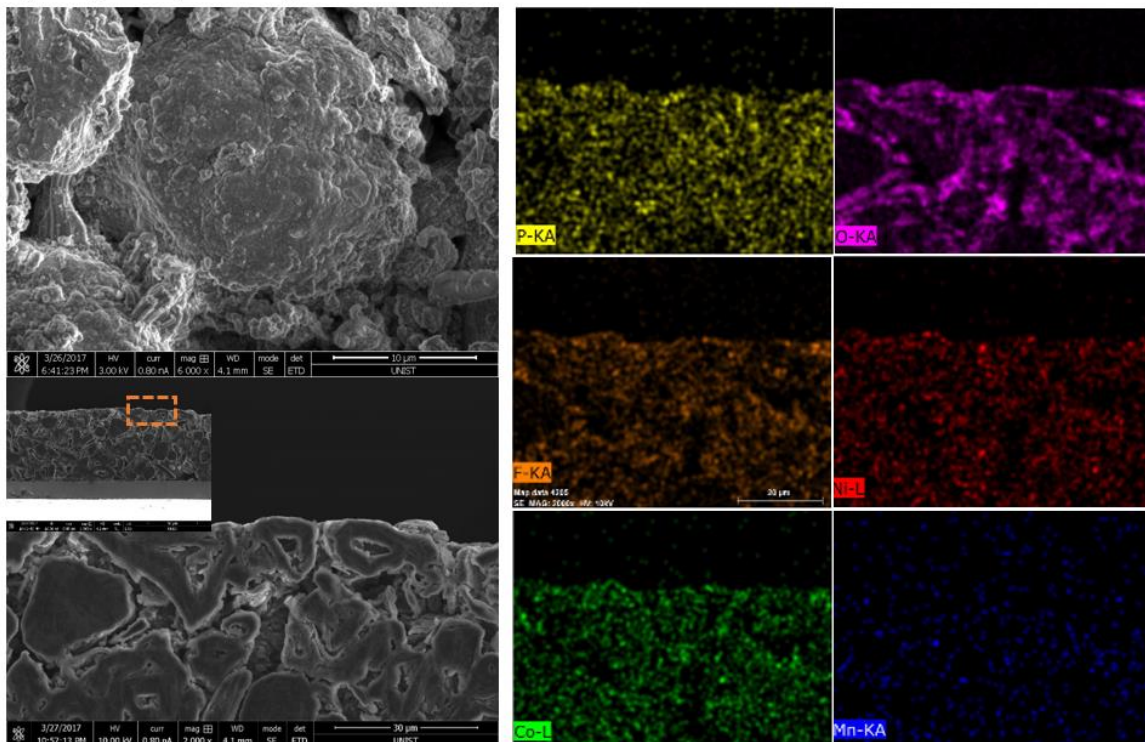
Figure 27. SEM images and EDS of graphite surface and cross-sectional image of **a)** NCM/graphite sample and **b)** G-NCM/graphite sample.

a) Graphite (NCM)
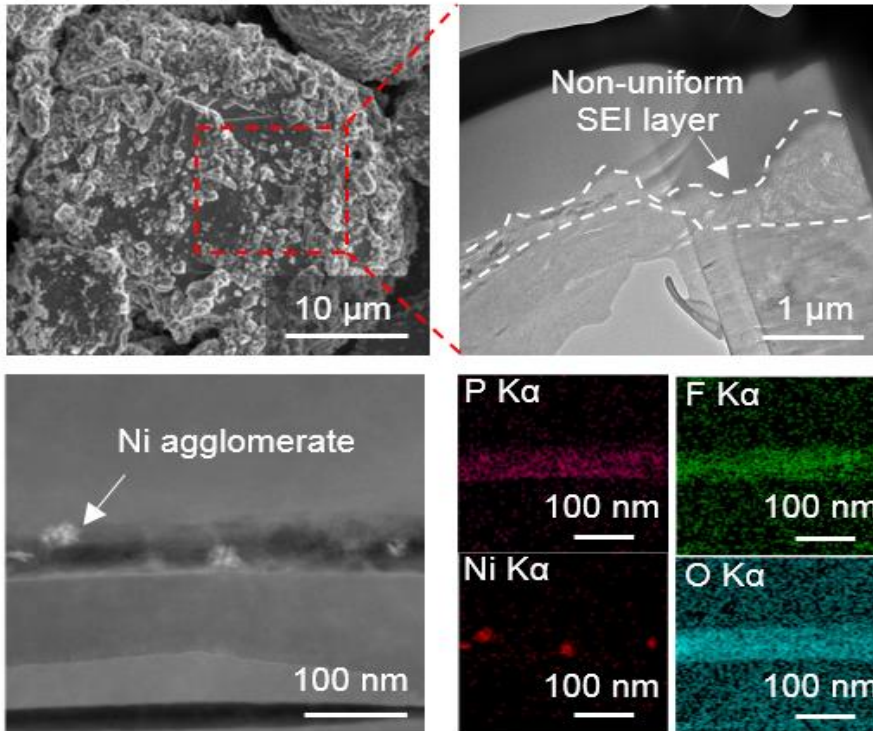
b) Graphite (G-NCM)
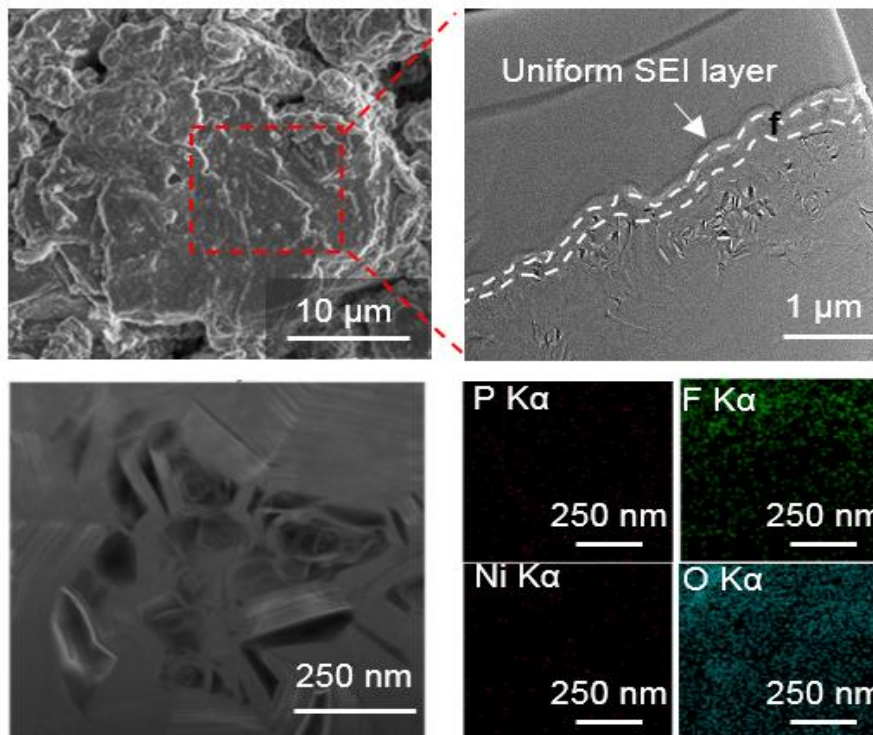
Figure 28. TEM images and EDS of graphite **a)** NCM/graphite sample and **b)** G-NCM/graphite sample**.**
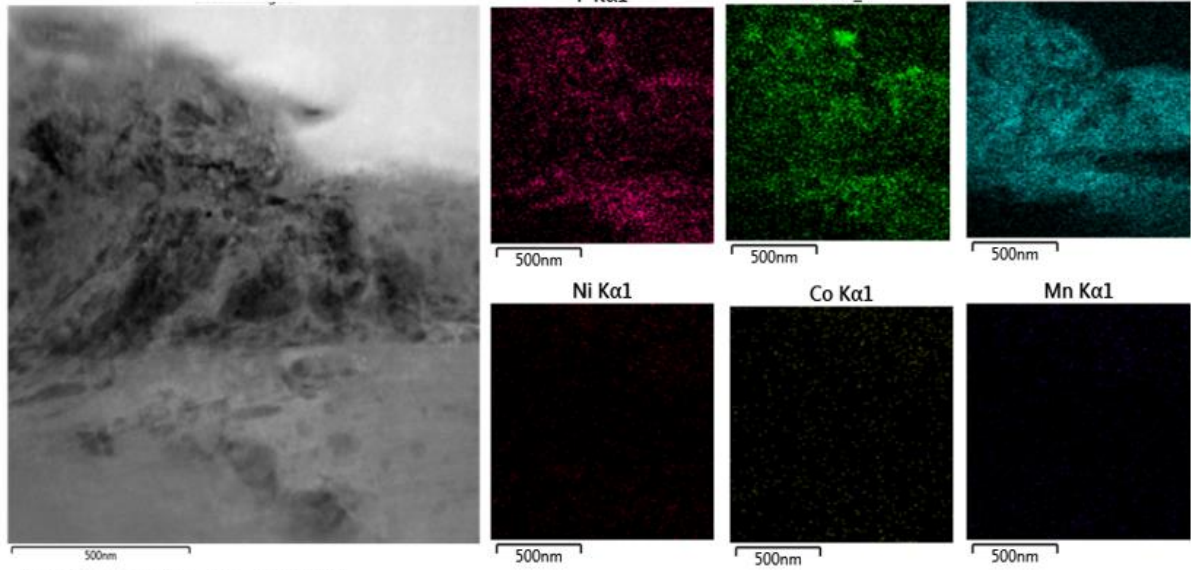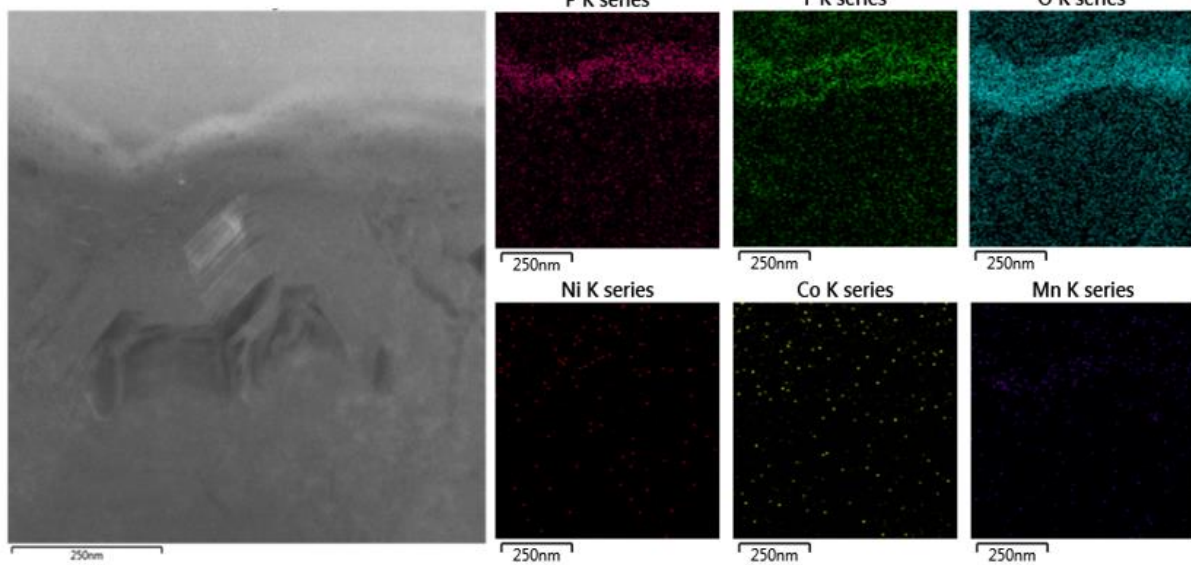
Figure 29. TEM images and EDS of SEI layer of **a)** NCM/graphite sample and **b)** G-NCM/graphite sample**.**
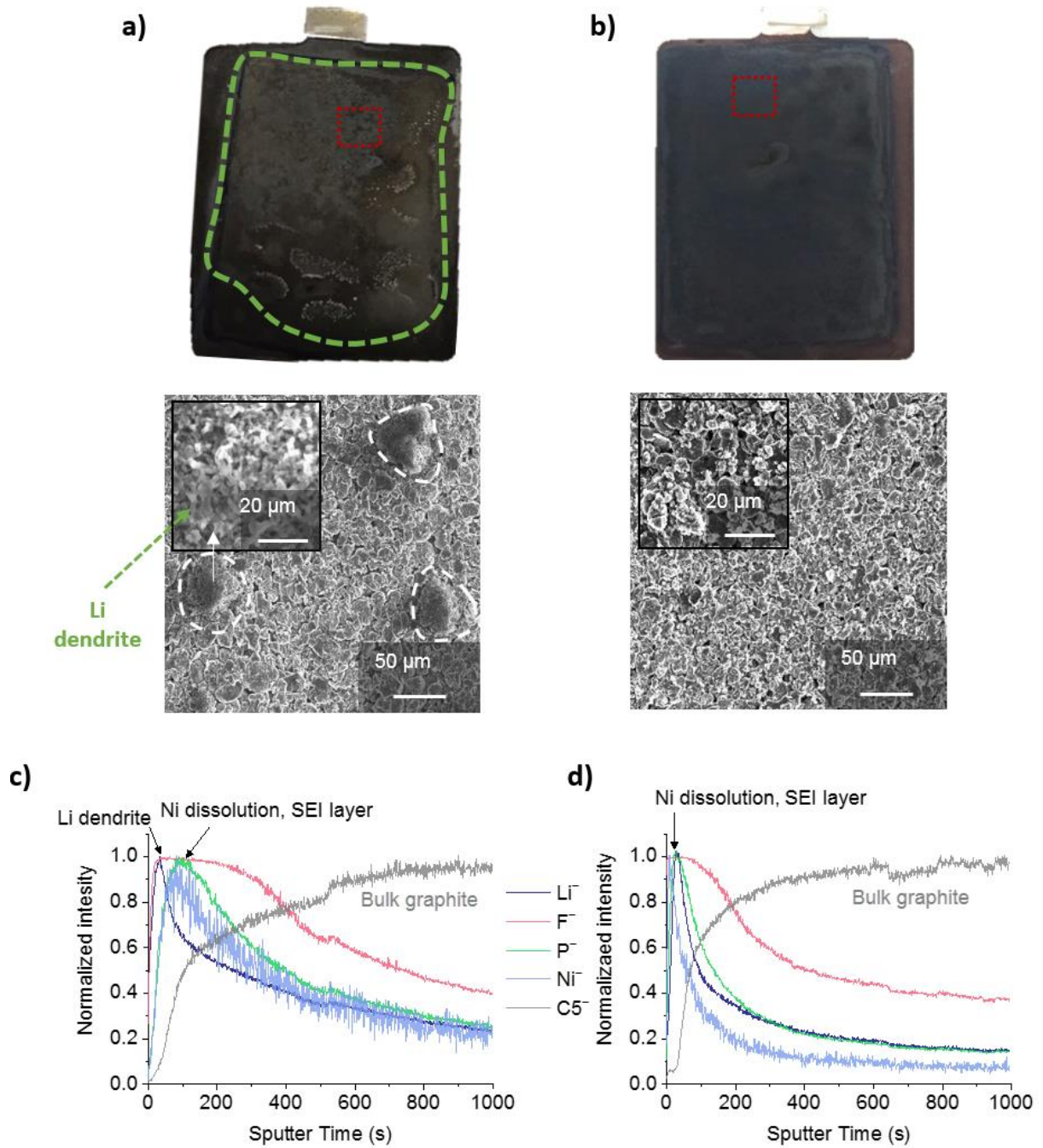
Figure 30. SEM image of graphite **a)** NCM/graphite sample and **b)** G-NCM/graphite sample. TOF-SIMS depth profiling data of **c)** NCM/graphite sample and **d)** G-NCM/graphite sample.

IV. Conclusion

In summary, the $LiNi_{0.8}Co_{0.1}Mn_{0.1}O_2$ cathode material was treated with cobalt-rich materials (G-treatment, G-NCM) which was a product of the reaction between the residual lithium and cobalt precursor. The cobalt-rich phase can control the degree of transition metal dissolution and improve structural stability in cathode material through transition metal gradient on the primary particles. Moreover, suppressed transition metal dissolution can contribute to form stable and thin SEI layer on the surface of the anode. Especially, G-treatment was more effective at high temperature in cycling performance of both half-cell results and full-cell results. Structural stability of G-NCM was confirmed via HR-TEM and STEM results. In G-NCM, the cation mixing layer was diminished compared with NCM after cycling test. Also, reduced transition metal dissolution was confirmed via EDS results of the cathode ToF-SIMS results of the anode. This newly developed Ni-rich cathode material have high capacity and high stability at high temperature as well as improved the charge-discharge cycling performance compared to those of the NCM.

V. Reference

1.	Tarascon, J. M.; Armand, M., Issues and challenges facing rechargeable lithium batteries. *Nature* **2001**, *414* (6861), 359-367.

2.	Goodenough, J. B.; Park, K. S., The Li-Ion Rechargeable Battery: A Perspective. *Journal of the American Chemical Society* **2013**, *135* (4), 1167-1176.

3.	Dunn, B.; Kamath, H.; Tarascon, J. M., Electrical Energy Storage for the Grid: A Battery of Choices. *Science* **2011**, *334* (6058), 928-935.

4.	(a) Xu, B.; Qian, D. N.; Wang, Z. Y.; Meng, Y. S. L., Recent progress in cathode materials research for advanced lithium ion batteries. *Materials Science & Engineering R-Reports* **2012,** *73* (5-6), 51-65; (b) Ellis, B. L.; Lee, K. T.; Nazar, L. F., Positive Electrode Materials for Li-Ion and Li-Batteries. *Chemistry of Materials* **2010**, *22* (3), 691-714; (c) Whittingham, M. S., Lithium batteries and cathode materials. *Chemical Reviews* **2004**, *104* (10), 4271-4301.

5.	Ohzuku, T.; Ueda, A., WHY TRANSITION-METAL (DI) OXIDES ARE THE MOST ATTRACTIVE MATERIALS FOR BATTERIES. *Solid State Ionics* **1994**, *69* (3-4), 201-211.

6.	Ohzuku, T.; Ueda, A.; Nagayama, M., ELECTROCHEMISTRY AND STRUCTURAL CHEMISTRY OF LINIO2 (R(3)OVER-BAR-M) FOR 4 VOLT SECONDARY LITHIUM CELLS. *Journal of the Electrochemical Society* **1993**, *140* (7), 1862-1870.

7.	Julien, C.M.; Mauger, A.; Zaghib, K.; Groult, H. Comparative Issues of Cathode Materials for Li-Ion Batteries. *Inorganics* **2014**, *2*, 132-154. .

8.	Goodenough, J. B.; Kim, Y., Challenges for Rechargeable Li Batteries. *Chemistry of Materials* **2010**, *22* (3), 587-603.

9.	Manthiram, A.; Murugan, A. V.; Sarkar, A.; Muraliganth, T., Nanostructured electrode materials for electrochemical energy storage and conversion. *Energy & Environmental Science* **2008**, *1* (6), 621-638.

10.	(a) Li, W.; Reimers, J. N.; Dahn, J. R., IN-SITU X-RAY-DIFFRACTION AND ELECTROCHEMICAL STUDIES OF LI-1-XNIO2. *Solid State Ionics* **1993**, *67* (1-2), 123-130; (b) Arai, H.; Okada, S.; Ohtsuka, H.; Ichimura, M.; Yamaki, J., CHARACTERIZATION AND CATHODE PERFORMANCE OF LI-1-XNI1+XO2 PREPARED WITH THE EXCESS LITHIUM METHOD. *Solid State Ionics* **1995**, *80* (3-4), 261-269; (c) Peres, J. P.; Weill, F.; Delmas, C., Lithium/vacancy ordering in the monoclinic LixNiO2 (0.50 <= x <= 0.75) solid solution. *Solid State Ionics* **1999**, *116* (1-2), 19-27.

11.	Delmas, C.; Croguennec, L., Layered Li(Ni, M)O-2 systems as the cathode material in lithium-

ion batteries. *MRS Bull.* **2002**, *27* (8), 608-612.

12.   Dahn, J. R.; Vonsacken, U.; Michal, C. A., STRUCTURE AND ELECTROCHEMISTRY OF LI1+/-YNIO2 AND A NEW LI2NIO2 PHASE WITH THE NI(OH)2 STRUCTURE. *Solid State Ionics* **1990**, *44* (1-2), 87-97.

13.   (a) Koyama, Y.; Arai, H.; Tanaka, I.; Uchimoto, Y.; Ogumi, Z., Defect Chemistry in Layered LiMO2 (M = Co, Ni, Mn, and Li1/3Mn2/3) by First-Principles Calculations. *Chemistry of Materials* **2012**, *24* (20), 3886-3894; (b) Yu, H. J.; Qian, Y. M.; Otani, M. R.; Tang, D. M.; Guo, S. H.; Zhu, Y. B.; Zhou, H. S., Study of the lithium/nickel ions exchange in the layered LiNi0.42Mn0.42Co0.16O2 cathode material for lithium ion batteries: experimental and first-principles calculations. *Energy & Environmental Science* **2014**, *7* (3), 1068-1078.

14.   (a) Huang, Z. L.; Gao, J.; He, X. M.; Li, J. J.; Jiang, C. Y., Well-ordered spherical LiNixCo(1-2x)MnxO2 cathode materials synthesized from cobolt concentration-gradient precursors. *J. Power Sources* **2012**, *202*, 284-290; (b) Zhang, B.; Li, L. J.; Zheng, J. C., Characterization of multiple metals (Cr, Mg) substituted LiNi0.8Co0.1Mn0.1O2 cathode materials for lithium ion battery. *Journal of Alloys and Compounds* **2012**, *520*, 190-194.

15.   Lee, J.; Urban, A.; Li, X.; Su, D.; Hautier, G.; Ceder, G., Unlocking the Potential of Cation-Disordered Oxides for Rechargeable Lithium Batteries. *Science* **2014**, *343* (6170), 519-522.

16.   (a) Liu, W.; Oh, P.; Liu, X.; Lee, M. J.; Cho, W.; Chae, S.; Kim, Y.; Cho, J., Nickel-Rich Layered Lithium Transition-Metal Oxide for High-Energy Lithium-Ion Batteries. *Angew. Chem.-Int. Edit.* **2015**, *54* (15), 4440-4457; (b) Cheng, C. X.; Tan, L.; Liu, H. W.; Huang, X. T., High rate performances of the cathode material LiNi1/3Co1/3Mn1/3O2 synthesized using low temperature hydroxide precipitation. *Materials Research Bulletin* **2011**, *46* (11), 2032-2035.

17.   (a) Ohzuku, T.; Ueda, A.; Nagayama, M.; Iwakoshi, Y.; Komori, H., COMPARATIVE-STUDY OF LICOO2, LINI1/2CO1/2O2 AND LINIO2 FOR 4-VOLT SECONDARY LITHIUM CELLS. *Electrochim. Acta* **1993**, *38* (9), 1159-1167; (b) Jung, S. K.; Gwon, H.; Hong, J.; Park, K. Y.; Seo, D. H.; Kim, H.; Hyun, J.; Yang, W.; Kang, K., Understanding the Degradation Mechanisms of LiNi0.5Co0.2Mn0.3O2 Cathode Material in Lithium Ion Batteries. *Advanced Energy Materials* **2014**, *4* (1).

18.   Cho, J. P.; Jung, H. S.; Park, Y. C.; Kim, G. B.; Lim, H. S., Electrochemical properties and thermal stability of LiaNi1-xCoxO2 cathode materials. *Journal of the Electrochemical Society* **2000**, *147* (1), 15-20.

19.   Dahn, J. R.; Fuller, E. W.; Obrovac, M.; Vonsacken, U., THERMAL-STABILITY OF LIXCOO2, LIXNIO2 AND LAMBDA-MNO2 AND CONSEQUENCES FOR THE SAFETY OF LI-ION CELLS. *Solid State Ionics* **1994**, *69* (3-4), 265-270.

20.   MacNeil, D. D.; Lu, Z. H.; Chen, Z. H.; Dahn, J. R., A comparison of the electrode/electrolyte reaction at elevated temperatures for various Li-ion battery cathodes. *J. Power Sources* **2002**, *108* (1-2), 8-14.

21.   (a) Aurbach, D.; Eineli, Y.; Markovsky, B.; Zaban, A.; Luski, S.; Carmeli, Y.; Yamin, H., THE STUDY OF ELECTROLYTE-SOLUTIONS BASED ON ETHYLENE AND DIETHYL CARBONATES FOR RECHARGEABLE LI BATTERIES .2. GRAPHITE-ELECTRODES. *Journal of the Electrochemical Society* **1995**, *142* (9), 2882-2890; (b) Cho, D. H.; Jo, C. H.; Cho, W.; Kim, Y. J.; Yashiro, H.; Sun, Y. K.; Myung, S. T., Effect of Residual Lithium Compounds on Layer Ni-Rich Li Ni0.7Mn0.3 O-2. *Journal of the Electrochemical Society* **2014**, *161* (6), A920-A926.

22.   (a) Chen, J. G.; Devries, B. D.; Lewandowski, J. T.; Hall, R. B., DIRECT DIFFERENTIATION OF SURFACE AND BULK COMPOSITIONS OF POWDER CATALYSTS - APPLICATION OF ELECTRON-YIELD AND FLUORESCENCE-YIELD NEXAFS TO LIXNI1-XO. *Catalysis Letters* **1994**, *23* (1-2), 25-35; (b) Nohma, T.; Kurokawa, H.; Uehara, M.; Takahashi, M.; Nishio, K.; Saito, T., ELECTROCHEMICAL CHARACTERISTICS OF LINIO2 AND LICOO2 AS A POSITIVE MATERIAL FOR LITHIUM SECONDARY BATTERIES. *J. Power Sources* **1995**, *54* (2), 522-524; (c) Chang, C. C.; Scarr, N.; Kumta, P. N., Synthesis and electrochemical characterization of LiMO2 (M = Ni, Ni0.75Co0.25) for rechargeable lithium ion batteries. *Solid State Ionics* **1998**, *112* (3-4), 329-344.

23.   (a) Liu, H. S.; Yang, Y.; Zhang, J. J., Investigation and improvement on the storage property of LiNi0.8Co0.2O2 as a cathode material for lithium-ion batteries. *J. Power Sources* **2006**, *162* (1), 644-650; (b) Liu, H. S.; Yang, Y.; Zhang, J. J., Reaction mechanism and kinetics of lithium ion battery cathode material LiNiO2 with CO2. *J. Power Sources* **2007**, *173* (1), 556-561; (c) Kim, Y., Mechanism of gas evolution from the cathode of lithium-ion batteries at the initial stage of high-temperature storage. *Journal of Materials Science* **2013**, *48* (24), 8547-8551.

24.   (a) Aurbach, D., THE ELECTROCHEMICAL-BEHAVIOR OF LITHIUM SALT-SOLUTIONS OF GAMMA-BUTYROLACTONE WITH NOBLE-METAL ELECTRODES. *Journal of the Electrochemical Society* **1989**, *136* (4), 906-913; (b) Edstrom, K.; Gustafsson, T.; Thomas, J. O., The cathode-electrolyte interface in the Li-ion battery. *Electrochim. Acta* **2004**, *50* (2-3), 397-403.

25.   (a) Jo, M.; Noh, M.; Oh, P.; Kim, Y.; Cho, J., A New High Power LiNi0.81Co0.1Al0.09O2 Cathode Material for Lithium-Ion Batteries. *Advanced Energy Materials* **2014**, *4* (13); (b) Guilmard, M.; Rougier, A.; Grune, A.; Croguennec, L.; Delmas, C., Effects of aluminum on the structural and electrochemical properties of LiNiO2. *J. Power Sources* **2003**, *115* (2), 305-314.

26.   Zhecheva, E.; Stoyanova, R., STABILIZATION OF THE LAYERED CRYSTAL-STRUCTURE OF LINIO2 BY CO-SUBSTITUTION. *Solid State Ionics* **1993**, *66* (1-2), 143-149.

27.   Chen, H. R.; Dawson, J. A.; Harding, J. H., Effects of cationic substitution on structural defects in layered cathode materials LiNiO2. *Journal of Materials Chemistry A* **2014**, *2* (21), 7988-7996.

28.   Montoro, L. A.; Abbate, M.; Almeida, E. C.; Rosolen, J. M., Electronic structure of the transition metal ions in LiCoO2, LiNiO2 and LiCo0.5Ni0.5O2. *Chemical Physics Letters* **1999**, *309* (1-2), 14-18.

29.   Makimura, Y.; Ohzuku, T., Lithium insertion material of LiNi1/2Mn1/2O2 for advanced lithium-ion batteries. *J. Power Sources* **2003**, *119*, 156-160.

30.   Guilmard, M.; Croguennec, L.; Delmas, C., Effects of manganese substitution for nickel on the structural and electrochemical properties of LiNiO2. *Journal of the Electrochemical Society* **2003**, *150* (10), A1287-A1293.

31.   Koyama, Y.; Tanaka, I.; Adachi, H.; Makimura, Y.; Ohzuku, T., Crystal and electronic structures of superstructural Li1-x Co1/3Ni1/3Mn1/3 O-2 (0 <= x <= 1). *J. Power Sources* **2003**, *119*, 644-648.

32.   Ohzuku, T.; Makimura, Y., Layered lithium insertion material of LiCo1/3Ni1/3Mn1/3O2 for lithium-ion batteries. *Chemistry Letters* **2001**,   (7), 642-643.

33.   Yabuuchi, N.; Ohzuku, T., Novel lithium insertion material of LiCo1/3Ni1/3Mn1/3O2 for advanced lithium-ion batteries. *J. Power Sources* **2003**, *119*, 171-174.

34.   Sun, Y. K.; Myung, S. T.; Park, B. C.; Prakash, J.; Belharouak, I.; Amine, K., High-energy cathode material for long-life and safe lithium batteries. *Nature Materials* **2009**, *8* (4), 320-324.

35.   (a) Wu, S. H.; Yang, C. W., Preparation of LiNi0.8CO0.2O2-based cathode materials for lithium batteries by a co-precipitation method. *J. Power Sources* **2005**, *146* (1-2), 270-274; (b) Kim, M. H.; Shin, H. S.; Shin, D.; Sun, Y. K., Synthesis and electrochemical properties of Li Ni0.8Co0.1Mn0.1 O-2 and Li Ni0.8Co0.2 O-2 via co-precipitation. *J. Power Sources* **2006**, *159* (2), 1328-1333; (c) Zhang, Y.; Cao, H.; Zhang, J.; Xia, B. J., Synthesis of LiNi0.6Co0.2Mn0.2O2 cathode material by a carbonate co-precipitation method and its electrochemical characterization. *Solid State Ionics* **2006**, *177* (37-38), 3303-3307.

36.   Obrovac, M. N.; Mao, O.; Dahn, J. R., Structure and electrochemistry of LiMO2, (M = Ti, Mn, Fe, Co, Ni) prepared by mechanochemical synthesis. *Solid State Ionics* **1998**, *112* (1-2), 9-19.